SPORE Mission Design

Nicole Bauer
Georgia Institute of Technology, Atlanta, GA, 30332

Small Probes for Orbital Return of Experiments (SPORE), provides an on-orbit and re-entry platform for a range of biological, thermal protection system (TPS) characterization, and material science experiments. This platform will provide the capability for 1-4 weeks of on-orbit flight operations for experiments with comparable mass and volumes laid out by the 1U and 2U cubesat guidelines. The platform will accommodate return from low earth orbit (LEO) and geosynchronous transfer orbit (GTO) to maximize the science potential. Packaging models and mass budgets were created for the SPORE entry vehicles. In addition, analyses were completed to construct the SPORE mission design. Orbital trajectory and maneuvers were modeled for the LEO and GTO missions. A re-entry architecture was designed to meet the requirements set by the range of payloads, orbits, and entry vehicle sizes inherent in the SPORE mission concept. The selected entry, descent, and landing (EDL) architecture was validated and modeled using 3-DOF and 6-DOF software. A thermal soak-back analysis was used to generate a temperature profile for the payload, and a Monte Carlo analysis was completed on this architecture to assess landing footprint. Results from the landing dispersion analysis confirm current landing site selections and help establish recovery procedures.

Nomenclature

$\mathcal{S}$ = Stefan-Boltzmann constant (5.67e-8 W/cm^2/K^4)
$\mathcal{e}$ = Surface emissivity
a = Semi-major Axis
ACS = Attitude Control System
D_{max} = Maximum entry vehicle diameter (m)
DOF = Degree of Freedom
e = Eccentricity
EDL = Entry, Descent, and Landing
EME2000 = Earth-Centered Earth Mean Equator and Equinox of Epoch J2000
FIAT = Fully Implicit Ablation and Thermal Response program
Fixed = Earth-Centered Earth Mean Equator and Prime Meridian of Date
FPA = Flight Path Angle
GPS = Global Positioning System
GTO = Geosynchronous Transfer Orbit
i = Inclination
ISS = International Space Station
LEO = Low Earth Orbit
PD = Proportional Derivative
PICA = Phenolic Impregnated Carbon Ablator (TPS)
POST = Program to Optimize Simulated Trajectories
q_{conv} = Stagnation point convective heat flux (W/cm^2)
q_{rad} = Stagnation point radiative heat flux (W/cm^2)
q_{rerad} = Re-radiated heat flux (W/cm^2)
R = Radius
r_a = Apogee Altitude
r_p = Perigee Altitude
SPORE = Small Probes for Orbital Return of Experiments
STK = Satellite Tool Kit
TPS = Thermal Protection System
T_{surf} = TPS surface wall temperature (K)
u = Argument of Latitude
UTTR = Utah Test and Training Range
Γ = Flight Path Angle
δ = Latitude
θ = Right Ascension
λ = Longitude
ν = True Anomaly
Σ = Azimuth
φ = Declination
ω = Argument of Perigee
Ω = Right Ascension of the Ascending Node

Table of Contents

List of Figures

List of Tables

1 Introduction

Small Probes for Orbital Return of Experiments (SPORE) provides a scalable, modular on-orbit and re-entry platform for experiments related to thermal protection system (TPS) flight characterization, biological and life sciences, and material sciences. The SPORE platform accommodates payload volumes comparable to the 1-unit (1U) dimensions of 10x10x10 cm and two 2-Unit (2x2U) dimensions of 10x10x20 cm. SPORE can be launched as a primary or secondary payload. It offers 1-4 weeks of on-orbit flight operations and return from low-Earth orbit (LEO) including ISS-return missions and geosynchronous transfer orbit (GTO).

SPORE provides the opportunity to improve the technology readiness level of experimental TPS materials in order to reduce mass and other design margins. Potential biological experiments can take advantage the microgravity and radiation environment to help assess risks on human health. SPORE allots material science payloads the opportunity to perform low gravity construction tests and access to the radiation environment. SPORE addresses the need for low-cost access to an on-orbit microgravity and radiation environment, enabling experiments that require safe return to an Earth-based laboratory.

The primary design challenge for SPORE is establishing a mission design architecture capable of meeting the requirements set by multiple payloads, orbits, and vehicle sizes. This paper discusses requirements that lead to the selection of the nominal orbital and entry trajectories. Packaging and mass budgets are provided for the 1U and 2x2U vehicles. The baseline orbital trajectories are given along with nominal entry state and attitude profiles. The selected entry, descent, and landing (EDL) architecture has been validated with the three-degree-of-freedom (3 DOF) and 6 DOF models described. The 3 DOF models were developed by the Georgia Tech SPORE team and the six-DOF models use Program to Optimize Simulated Trajectories (POST) II software developed by NASA Langley[15,]5. The parachute model is explained in detail. A temperature profile of the payload is generated through a thermal soak back analysis to ensure the payload survives re-entry. A Monte Carlo analysis was completed on this architecture to assess landing footprint and evaluate design robustness. The Monte Carlo approach and results are described. Results from the landing dispersion analysis confirm current landing site selections and help establish recovery procedures.

2 Requirements

Although SPORE provides access to different orbits, payload types, and payload sizes, certain combinations lack customer demand. For the TPS testbed mission, the customer requires one-to-one (1:1) flight data comparison with arcjet tests forcing 1:1 geometric similitude between the arcjet model and SPORE vehicle. This constrains the outer diameter to 16 inches. As a result, only the 1U payload size is considered for TPS testbed missions. Similarly, the biological and materials science communities have shown more interest in a 2U payload since the additional volume provides room for both samples and support equipment. Therefore the 1U payload size is excluded from those two cases. Figure 1outlines the design space for the SPORE architecture.
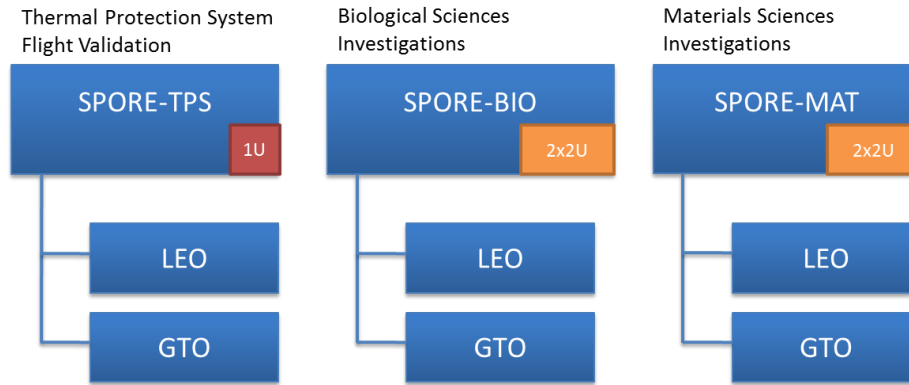
Figure 1. Diagram of SPORE design space

The LEO and GTO entry trajectories are constrained by the parameters given in Table 1. The appropriate payload type for each constraint is indicated in the last column of Table 1. The biological and material science payload requirements dictate the loading constraints. The maximum loading constraints refer to maximum linear accelerations experienced by the payload during re-entry for a given amount of time along any of the principal axes. In addition to these constraints, the biological and material science payloads cannot exceed 40 g during parachute deployment and landing4. The 40 g constraints are accounted for in the parachute sizing analysis.

Table 1: Entry trajectory requirements.

Maximum Loading for 100s (g's)4	9	BIO/MSE
Maximum Loading for 20s (g's)4	16	BIO/MSE
Maximum Loading (Parachute/Landing) (g's)4	40	BIO/MSE
Maximum Payload Temperature (°C)4	25	BIO/MSE
Target Interior Entry Vehicle Temperature (°C)3	0-50	TPS
Maximum Total Angle of Attack (°)1	5	TPS, BIO/MSE
Maximum Landing Ellipse Size (km)3	500 x 250	TPS, BIO/MSE
Maximum Entry Vehicle Diameter (m)3	0.4064	TPS
Maximum Impact Velocity (m/s)3	5	TPS
Target Peak Heating (W/cm^2)3	100-400	TPS (LEO)
	500-1000	TPS (GTO)
Target Stagnation Pressure (kPa)3	10-25	TPS (LEO)
	15-50	TPS (GTO)

The temperature of the payload is constrained to ensure the payload does not overheat during re-entry. The temperature constraint is addressed in the TPS and heat sink sizing analysis. The maximum total

angle of attack constraint ensures the vehicle is stable throughout all flight regimes. A 6DOF model of the SPORE entry trajectory assesses dynamic stability during the hypersonic, supersonic, and transonic entry regimes. The landing ellipse dimensions are dictated by the size of the landing site in Woomera, Australia. The landing ellipse constraint is verified through a dispersion analysis.

The 1U entry vehicle diameter is limited to 16 inches to create a one-to-one vehicle comparison between the TPS arc-jet test module and SPORE entry vehicle. To increase the scientific value of the TPS vehicle, additional requirements shown in Table 1 were imposed on the TPS entry trajectory. The stagnation point heat flux and pressure requirements were derived from Orion reference entry trajectories including return from ISS, lunar, and asteroid missions.

3   EV Geometry and Packaging

SPORE adopted the Mars Microprobe 45° sphere cone geometry designed by NASA Langley to simplify the re-entry architecture and ensure passive stability throughout hypersonic, supersonic, and subsonic re-entry phases[13]. The Mars Microprobe aeroshell shape consisted of a 45°spherecone forebody and a hemispherically-shaped back shell, with the radius of curvature located at the vehicle center of gravity for stability purposes9. The nose radius for the Mars Microprobe was $0.25*D_{max}$, and the shoulder radius was $0.1*D_{max}$, where D_{max} is the maximum diameter of the re-entry vehicle spherecone9. Figure 2and Figure 3depict the 1U and 2x2U packaging models. A mass budget is given for the 1U and 2x2U vehicles are given in

Table 2and Table 3respectively.
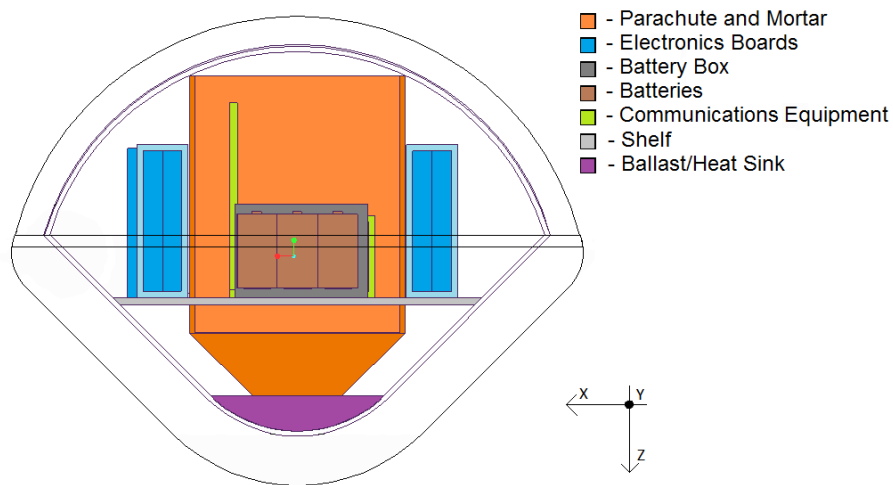
Figure 2.1U 16 inch diameter re-entry vehicle.

Table 2.Mass budget for 1U entry vehicle design.

1U Entry Vehicle Mass Budget	
Forebody structure (kg)	1.1
Backshell structure (kg)	1.23
Forebody TPS (kg)	1.36
Backshell TPS (kg)	0.43
Main parachute (kg)	1.06
Heatsink/Ballast (kg)	0.27
Shelf/Electronics Boxes/Payload (kg)	3.29
Entry Vehicle Total (kg)	**8.74**
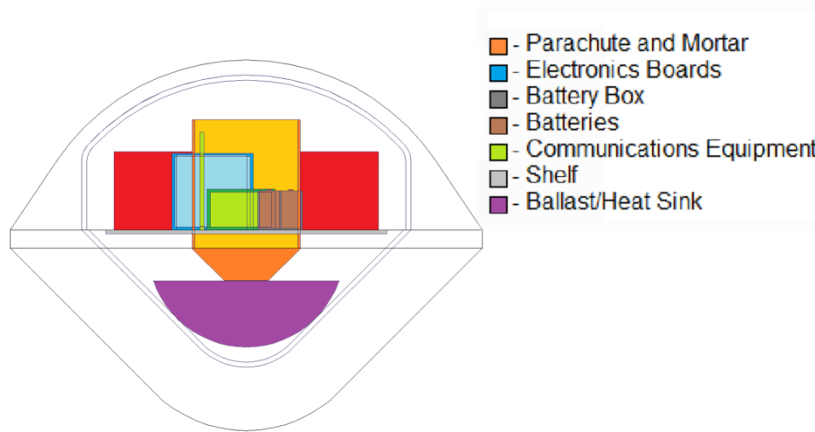
Figure 3.2x2U 24 inch diameter re-entry vehicle.

Table 3.Mass budget for 2x2U entry vehicle design

2x2U Entry Vehicle Mass Budget	
Forebody structure (kg)	3.19
Backshell structure (kg)	5.02
Forebody TPS (kg)	7.04
Backshell TPS (kg)	1.81
Main parachute (kg)	3.632
Heatsink/Ballast (kg)	4.87
Shelf/Electronics Boxes/Payload (kg)	6.74
Entry Vehicle Total (kg)	**32.302**

Research completed at NASA Langley estimated the center of gravity should be located at 34.6% of the diameter along the centerline of the vehicle to achieve passive stability9. Due to packaging constraints,

this center of gravity requirement cannot be met for the 1U and 2x2U vehicles. A 6DOF model of the SPORE entry trajectory was created using POSTII to assess dynamic stability during the hypersonic, supersonic, and transonic entry regimes. The CG location for the 1U and 2x2U vehicles is given in Table 4.Figure 4depicts the coordinate system to locate the CG.

Table 4: Center of gravity location of the 1U and 2U SPORE vehicles. These values were input in the POST model. The X_{CG}/D_{max} parameter provides comparison to the Mars Microprobe research completed at Langley9.

	X (mm)	Y (mm)	Z (mm)	X_{CG}/D_{max}(%)
1U	143.3	2.74	-1.89	37.1%
2x2U	245.3	2.87	-1.05	40.6%
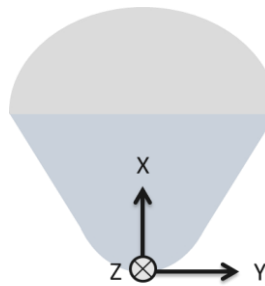
Figure 4.Coordinate system used to locate center of gravity.

The moment of inertia properties are needed for the 6 DOF model. These values are given in Table 5, Table 5 for the 1U and 2x2U vehicles respectively. The moment of inertias were calculated about the center of gravity using the coordinate system depicted in Figure 5.

Table 5.6 DOF vehicle moments of inertia for the 1U and 2x2U vehicles. These values were input in the POST model.

	I_{xx} (kg-m^2)	I_{yy} (kg-m^2)	I_{zz} (kg-m^2)
1U	0.1	0.082	0.089
2x2U	0.717	0.611	0.649
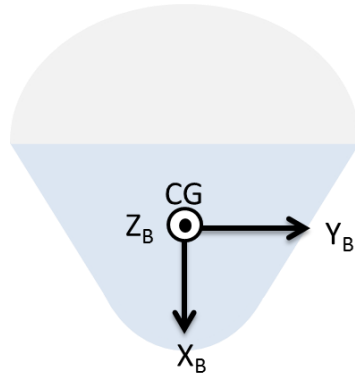
Figure 5. Coordinate system used to find the moments of inertia. This coordinate system is anchored at the vehicle's center of gravity. **The B subscript denotes the POST body axis 5**[.15].

4 SPORE Mission Design

The SPORE mission design can be broken into two components: on-orbit and re-entry. The coordinate frames and transformations needed to describe each of these components are defined in this section. The mission design for the 1U and 2x2U vehicles was constructed using 3 DOF and 6 DOF software, thermal analysis code, and parachute sizing relationships. These tools along with the resulting nominal orbital and entry trajectories are described here. Dispersions on the nominal entry state are discussed in reference to Monte Carlo analyses.

4.1 Coordinate Frames

The baseline LEO and GTO orbits are defined using classical orbital elements, the Earth-Centered Earth Mean Equator and Equinox of Epoch J2000 (EME2000) coordinate system, and the Earth-Centered Earth Mean Equator and Prime Meridian of Date (Fixed) coordinate system. All entry states are given in the spherical atmospheric relative coordinate system. The following sections catalog the coordinate frames and transformations used to describe the orbital and entry trajectories.

4.1.1 Classical Orbital Elements

The following orbital element definitions can be found in Reference 12.

Apogee Altitude (r_a) is the distance from the surface of the earth to the point farthest away from the prime focus of an elliptical orbit.

Perigee Altitude (r_p) is the distance from the surface of the earth to the point nearest to the prime focus of an elliptical orbit.

Eccentricity (e) is a constant that defines the shape of the conic orbit. Elliptical orbits have eccentricity between zero and one.

Semi-major Axis (a) is a constant that defines the size of the orbit. It spans half of the chord passing through both foci connecting apogee and perigee.

Argument of Perigee (ω) is the angle in the plane of the satellite's orbit, between the ascending node and the perigee measured in the direction of the satellite's motion.

RAAN (Ω) is the angle between X unit vector and the point where the satellite crosses through the equatorial plane in a northerly direction. The angle is measured clockwise when viewed from the north side of the equatorial plane.

Inclination (i) is the angle between the Z unit vector and the angular momentum vector of the orbit.

True Anomaly (υ): the angle, in the plane of the orbit, between periapsis and the position of the satellite at time t_0.

Argument of Latitude (u): The angle in the plane of the orbit between the ascending node and the radius vector a time t_0. The angle is used in place of true anomaly for circular orbits.

4.1.2   EME2000: Earth-Centered Earth Mean Equator and Equinox of Epoch J2000

The Earth-Centered Earth Mean Equator and Equinox of Epoch J2000 (EME2000) inertial reference system is a right-handed coordinate system defined as follows:

> Frame:
> > Reference body: Earth
> > Reference plane: Earth Mean Equator
> > Reference direction: Vernal Equinox
> > Reference time: Epoch J2000
>
> Center: Earth-Centered
> Type: Cartesian

Epoch J2000 is January 1, 2000 at 12:00:00 ET (Julian date 2451545.0).

Note: This coordinate system is referred to as "**J2000**" within the Satellite Tool Kit (STK) software.

4.1.3   Fixed: Earth-Centered Earth Mean Equator and Prime Meridian of Date

The Earth-Centered Earth Mean Equator and Prime Meridian of Date rotating reference system is a right-handed coordinate system defined as follows:

> Frame:
> > Reference body: Earth
> > Reference plane: Earth Mean Equator
> > Reference direction: Prime Meridian
> > Reference time: of date
>
> Center: Earth-Centered
> Type: Cartesian

Prime Meridian refers to the line of intersection between the Earth's equatorial plane and prime meridian plane. The reference direction (X-axis) is along this line and directed toward 0° longitude. Thus the Y-axis is fixed at 90° longitude and the Z-axis is directed through the north pole.

Note: This coordinate system is referred to as "**Fixed**" within the Satellite Tool Kit (STK) software. The STK transformation into this frame includes the effects of precession, nutation, and rotation, as well as pole wander and frame corrections. This coordinate system is also known as "**ECEF**" (Earth-Centered Earth-Fixed). However, the PESST transformation assumes a spherical Earth and only accounts for rotation.

4.1.4 Spherical Inertial Relative

Right Ascension (θ) is the angle from the INERTIAL X axis to the projection of the satellite position vector in the INERTIAL equatorial plane measured as positive in the direction of the Y axis. Ranges from 0 to 360 degrees where 0 degrees is at the Vernal Equinox.

Declination (ϕ) is the angle between the satellite position vector and the INERTIAL equatorial plane measured as positive toward the positive INERTIAL Z axis. Ranges from 90 to -90 degrees where 0 degrees is at the equator as seen from the center of the earth.

Radius (R) is magnitude of the INERTIAL position vector.

Flight Path Angle (Γ_i) is the angle between the velocity vector and the local horizontal measured positive towards the outward radial direction. Ranges from 90 to -90 degrees.

Azimuth (Σ_i) is the angle in the satellite local horizontal plane between the projection of the velocity vector onto this plane and the local north direction measured as positive in the clockwise direction. Ranges from 0 to 360 degrees.

Velocity (V_i) is the magnitude of the INERTIAL velocity vector

4.1.5 Spherical Atmospheric Relative

Longitude (λ) is the angle from the Prime Meridian to the projection of the satellite position vector in the BODY FIXED (rotating) equatorial plane measured as positive in the direction of the Y axis. Ranges between 0 to 360 degrees where 0 degrees is at the Prime Meridian.

Latitude (δ) is the angle between the satellite position vector and the BODY FIXED (rotating) equatorial plane measured as positive toward the positive BODY FIXED (rotating) Z axis. Ranges from 90 to -90 degrees where 0 degrees is at the equator.

Radius (R) is magnitude of the BODY FIXED (rotating) position vector.

Flight Path Angle (Γ_A) is the angle between the velocity vector and the local horizontal measured positive towards the outward radial direction. The local horizontal defined in the BODY FIXED (rotating) coordinate system. Ranges from 90 to -90 degrees.

Azimuth (Σ_A) is the angle in the satellite local horizontal plane between the projection of the velocity vector onto this plane and the local north direction measured as positive in the clockwise direction. The local horizontal defined in the BODY FIXED (rotating) coordinate system. Ranges from 0 to 360 degrees.

Velocity (V_A) is the magnitude of the BODY FIXED (rotating) velocity vector. This takes into account rotation of the earth relative to the satellite.

4.1.6 Coordinate Frame Transformations

Orbital Elements → EME2000
The perifocal *r* and *v* vectors are calculated from the orbital elements as follows. This transformation is covered in detail in Reference12.

$$\vec{R_w} = \frac{a(1-e^2)}{1+e\cos v}[(\cos v)\widehat{x_w} + (\sin v)\widehat{y_w}] \tag{1}$$

$$\vec{V_w} = \sqrt{\frac{398600}{a(1-e^2)}}[(-\sin v)\widehat{x_w} + (\cos v + e)\widehat{y_w}] \tag{2}$$

These vectors are transformed to a inertial (EME2000) coordinate system via the following 3-1-3 rotation. This transformation is covered in detail in Reference 12.

$$\vec{R}_{EME2000} = [R_3(\Omega)R_1(i)R_3(\omega)]\vec{R_w} \tag{3}$$

$$\vec{V}_{EME2000} = [R_3(\Omega)R_1(i)R_3(\omega)]\vec{V_w} \tag{4}$$

Where

$$R_1(\alpha) = \begin{bmatrix} 1 & 0 & 0 \\ 0 & \cos\alpha & \sin\alpha \\ 0 & -\sin\alpha & \cos\alpha \end{bmatrix} \tag{5}$$

$$R_3(\alpha) = \begin{bmatrix} \cos\alpha & \sin\alpha & 0 \\ -\sin\alpha & \cos\alpha & 0 \\ 0 & 0 & 1 \end{bmatrix} \tag{6}$$

Inertial (EME2000) → Orbital Elements
Use the following relationships to transfer an inertial (EME2000) *r* and *v* vector into orbital elements. This transformation is covered in detail in Reference 12.

$$\vec{h} = \vec{r} \times \vec{V} \tag{7}$$

$$n = \hat{Z} \times \vec{h} \tag{8}$$

$$e = \left\| \frac{1}{\mu}\left[\left(v^2 - \frac{\mu}{R}\right)\vec{R} - (\vec{R} \cdot \vec{V})\vec{V}\right] \right\| \tag{9}$$

$$\cos i = \frac{h_Z}{h} \ (i < 180, always) \tag{10}$$

$$\cos\Omega = \frac{n_X}{n} \ (If \ n_Y > 0 \ then \ \Omega < 180) \tag{11}$$

$$\cos \omega = \frac{\vec{n} \cdot \vec{e}}{ne} \text{ (If } e_Z > 0 \text{ then } \omega < 180)$$ (12)

$$\cos \nu = \frac{\vec{e} \cdot \vec{R}}{eR} \text{ (If } \vec{R} \cdot \vec{V} > 0 \text{ then } \upsilon < 180)$$ (13)

$$\cos u = \frac{\vec{n} \cdot \vec{R}}{nR} \text{ (If } R_Z > 0 \text{ then } u < 180)$$ (14)

Cartesian → Spherical Coordinates
The spherical coordinates (R, θ, φ, V$_i$, Γ$_i$, Σ$_i$) or (R, λ, δ, V$_A$, Γ$_A$, Σ$_A$) are related to the Cartesian coordinates (X, Y, Z, $\dot{X}, \dot{Y}, \dot{Z}$) in the following manner. To find atmospheric relative spherical coordinates use Fixed Cartesian coordinates. To find inertial relative spherical coordinates use EME2000 Cartesian coordinates.

$$R = \sqrt{X^2 + Y^2 + Z^2}$$ (15)

$$\phi \, or \, \delta = \text{asin}\frac{Z}{R}$$ (16)

$$\theta \, or \, \lambda = \text{atan}\frac{Y}{X}$$ (17)

$$M = \begin{bmatrix} \cos\phi\cos\theta & \cos\phi\sin\theta & \sin\phi \\ -\sin\theta & \cos\theta & 0 \\ -\sin\phi\cos\theta & -\sin\phi\sin\theta & \cos\phi \end{bmatrix}$$ (18)

$$\vec{V} = \left[\dot{X}^2 + \dot{Y}^2 + \dot{Z}^2 \right]$$ (19)

$$\vec{V}' = M\vec{V} = [\dot{X}', \dot{Y}', \dot{Z}']$$ (20)

$$\Gamma = \text{asin}\frac{\dot{X}'}{V}$$ (21)

$$\Sigma = \text{atan}\frac{\dot{Y}'}{\dot{Z}'}$$ (22)

Spherical → Cartesian
Use the following equations to calculate Cartesian coordinates from spherical. To get EME2000 Cartesian coordinates use inertial relative spherical coordinates. To get Fixed Cartesian coordinates use atmospheric relative spherical coordinates.

$$X = R \cos\phi \cos\theta$$ (23)
$$Y = R \cos\phi \sin\theta$$ (24)
$$Z = R \sin\phi$$ (25)
$$\dot{X}' = (V \sin\Gamma)$$ (26)
$$\dot{Y}' = (V \cos\Gamma \sin\Sigma)$$ (27)
$$\dot{Z}' = (V \cos\Gamma \cos\Sigma)$$ (28)

$$\vec{V'} = [\dot{X}', \dot{Y}', \dot{Z}'] \qquad (29)$$
$$\vec{V} = M^{-1}\vec{V'} \qquad (30)$$

Inertial → Fixed

As seen in Equation 31 and 32, rotate the inertial coordinate system by angle α to transform velocity and position into a fixed coordinate system. The following method was used for PESST to find the atmospheric relative position and velocity.

$$\vec{V_F} = \begin{bmatrix} \cos\alpha & \sin\alpha & 0 \\ -\sin\alpha & \cos\alpha & 0 \\ 0 & 0 & 1 \end{bmatrix} \left(\vec{V_I} - \Omega_E\hat{Z} \times \vec{R_I} \right) \qquad (31)$$

$$\vec{R_F} = \begin{bmatrix} \cos\alpha & \sin\alpha & 0 \\ -\sin\alpha & \cos\alpha & 0 \\ 0 & 0 & 1 \end{bmatrix} \vec{R_I} \qquad (32)$$

The angle α is given by the following equation.

$$\alpha = \alpha_0 + t\Omega_E \qquad (16)$$

Here α_0 is the initial angle between the inertial and fixed x-axes (at time t_0), Ω_E is the rotation of the earth in degrees per second (~0.0042), and *t* is the amount of time elapsed in seconds since t_0. For a start time of 9 Feb 2011 17:00:00.000 UTCG as specified in the STK model, α_0 is equal to 34.294°. The above transformation does not take into account the effects of precession and nutation. Therefore it is not equivalent to the STK transformation.

Fixed → Inertial

Use the transpose of the rotation matrix given in Equation 32 to transfer between fixed and inertial axes. These relations are given in Equation 33 and 34.

$$\vec{R_I} = \begin{bmatrix} \cos\alpha & -\sin\alpha & 0 \\ \sin\alpha & \cos\alpha & 0 \\ 0 & 0 & 1 \end{bmatrix} \vec{R_F} \qquad (33)$$

$$\vec{V_I} = \begin{bmatrix} \cos\alpha & -\sin\alpha & 0 \\ \sin\alpha & \cos\alpha & 0 \\ 0 & 0 & 1 \end{bmatrix} \left(\vec{V_F} + \Omega_E\hat{Z} \times \vec{R_F} \right) \qquad (34)$$

The transformation in Equation 33 and 34 does not take into account the effects of precession and nutation. Therefore it is not equivalent to the STK transformation.

4.2 Baseline Orbital Trajectories

The LEO and GTO trajectories can be found in Table 6, Table 7, and

Table 8.The altitude of the LEO trajectory is 600 km to reduce the amount of orbital decay over the mission lifetime and the inclination is 90° to attract potential biological payloads. The GTO trajectory was established from the reference trajectory of the Atlas Launch vehicle. For a GTO trajectory, most launch vehicles do not perform an additional burn to zero the inclination at apoapsis. Therefore the SPORE GTO reference trajectory has an inclination equal to that of Cape Canaveral. Periapsis altitude was established from the Atlas launch vehicle trajectory. Specifications for other launch vehicles were comparable.

Table 6: Classical Orbital Elements for LEO and GTO reference orbits.

Classical Orbital Elements	Units	LEO	GTO
Apogee Altitude (ra)	km	600.00	35941.00
Perigee Altitude(rp)	km	600.00	167.00
Eccentricity (e)	--	0	0.73
Semi-major Axis (a)	km	6978.00	24432.10
Argument of Perigee (ω)	deg	--	180.00
RAAN (Ω)	deg	0.00	0
Inclination (i)	deg	90.00	28.50
True Anomaly (v)	deg	--	0
Argument of Longitude (u)	deg	0	--

Table 7: LEO and GTO reference orbits defined in the EME2000 coordinate system.

EME2000 Coordinate System	Units	LEO	GTO
X (Position)	km	6978.00	-6545.10
Y (Position)	km	0.00	0.00
Z (Position)	km	0.00	0.00
$\dot{X}$ (Velocity)	km/s	0.00	0.00
$\dot{Y}$ (Velocity)	km/s	0.00	-9.03
$\dot{Z}$ (Velocity)	km/s	7.56	-4.90

Table 8: LEO and GTO reference orbits defined in the Fixed coordinate system.

Fixed Coordinate System	Units	LEO	GTO
X (Position)	km	5765.00	-5407.30
Y (Position)	km	-3931.80	3687.80
Z (Position)	km	0.00	0.00
$\dot{X}$ (Velocity)	km/s	-0.29	-4.82
$\dot{Y}$ (Velocity)	km/s	-0.42	-7.06
$\dot{Z}$ (Velocity)	km/s	7.56	-4.90

4.3   Deorbit Burn[2] *(analysis completed by Matthew Nehrenz)*

The deorbit burn is performed by a constant thrust, 63 N thruster on the service module. The LEO and GTO orbits will follow a nominal trajectory using a trajectory tracking PD guidance controller. The nominal trajectory is built by applying thrust in the opposite direction of the vehicle's velocity until the desired amount of delta-V has been attained; since the burn is short, this approach closely approximates an impulsive maneuver. After the completion of the burn, the attitude control system (ACS) on the service module will orient the vehicle for re-entry. Shortly before re-entry, the service module will separate from the entry vehicle. The goal of the following simulation is to characterize the vehicle's state uncertainty at re-entry due to errors in the ACS, guidance system, and GPS. The two main sources of error contributing to the guidance system that are modeled here are the ACS (which controls the orientation of the thrust vector) and the GPS.

For an on-orbit maneuver, a good estimate for ACS accuracy is a 1° pointing error. To see how this pointing error affects the guidance system error, a Matlab program was written that simulates an attitude controller operating within a larger guidance control loop. The control law used here is a PD controller that aligns a designated vehicle axis with some vector in vehicle coordinates. To apply this approach to trajectory tracking, the control law aligns the vehicle's thruster axis with the desired thrust direction supplied by the guidance system. The ACS runs at 10 Hz while the guidance system operates at 1 Hz; within each guidance time step, the attitude controller is keeping the thrust vector in proper orientation. The simulation uncouples the rotational dynamics from the translational dynamics—for the duration of the outer guidance loop, the attitude portion runs a 3 DOF simulation and saves the resulting thrust vector with error to be applied over that guidance time step. Uncoupling the rotational and translational dynamics allowed for easy application of the random attitude errors that produced an ACS pointing accuracy of 1°. Figure 6shows the simulation's block diagram.
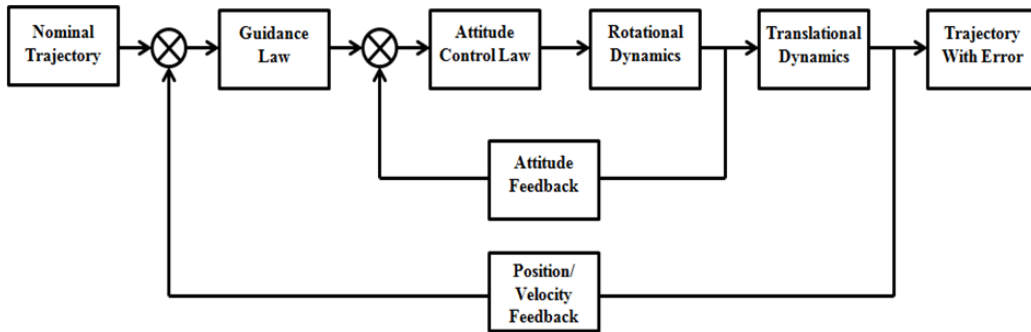
Figure 6. Deorbit simulation block diagram

Since the rotational dynamics are uncoupled from the translational dynamics, the simulation is not a 6 DOF, but is a 3+3 DOF simulation.

The other source of error added into the simulation was GPS position and velocity error. The uncertainties used for this analysis are taken from a GPS receiver in use on other small satellites. The position error is 1.8 m, and the velocity error is 0.03 m/s. Now that random errors in the guidance system have been characterized, a Monte Carlo analysis can be wrapped around the simulation to obtain uncertainties at the point of re-entry due to the guidance system. For each orbit, a 1000 run Monte Carlo was performed and the result 3-σ uncertainties are displayed in Table 9.

Table 9: 3-σ entry state uncertainties

	LEO	ISS	GTO
Flight Path Angle (deg)	0.0053	0.0036	0.0111
Velocity (m/s)	0.3393	0.0379	0.0032
Heading (deg)	0.0181	0.0189	0.004
Latitude (deg)	0.2401	0.1176	0.0235
Longitude (deg)	0.1663	0.4993	0.0121

4.4   Separation[2] *(written with the help of Matthew Nehrenz)*

Once the deorbit burn is executed, the service module ADCS reorients the vehicle to have a zero angle of attack at entry interface. Prior to entry interface, the service module releases the entry vehicle via a spring mechanism that is currently in design. The entry vehicle imparts a separation velocity between the service module and the entry vehicle; after a sufficient amount of clearance is obtained between the two vehicles, the service module performs a lateral maneuver to avoid recontact with the service module. Exact separation distances and release time will be decided after further analysis is performed. Figure 72 illustrates this sequence of events.
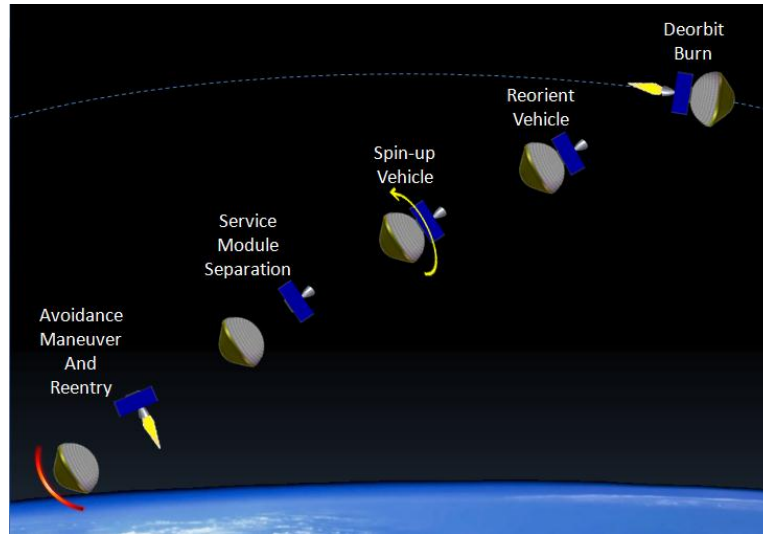
Figure 7.Separation sequence of events[2.]

4.5   EDL Sequence of Events

The SPORE entry vehicle will separate from the service module after the de-orbit maneuver is executed. The deployment attitude targets zero angle-of-attack at entry with respect to the atmosphere-relative velocity vector. The general EDL sequence of events for SPORE is as follows. Atmospheric entry occurs at a radius of 6,503 km (altitude of 125 km). Peak heating and maximum deceleration are experienced during the hypersonic regime, where the TPS is exposed to the target aerothermal environment. The parachute is deployed after transition to subsonic flight. The heatshield does not need to be jettisoned since the payload is thermally isolated from the heatshield soak-back by an aluminum heat sink. The vehicle approaches terminal velocity on the parachute prior to impact. Impact velocities vary based upon the vehicle configuration. A UHF beacon signal is transmitted throughout EDL to aid in the recovery process. Recovery is required to occur within 24 hours of touchdown. Figure 1 details the baseline EDL sequence of events for SPORE.
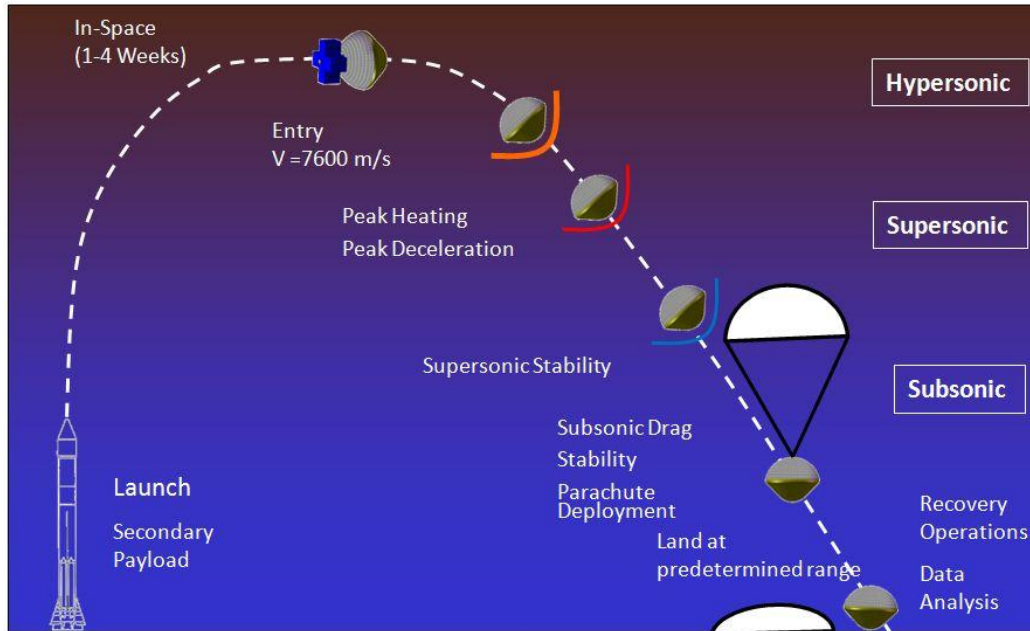
Figure 8.SPORE EDL Sequence of events.[3]

4.6 Define baseline entry trajectories

The 1U baseline trajectories that meet the TPS requirements are given in Table 10. Figure 9, Figure 10, Figure 11, and Figure 12 illustrate that the requirements are met. To reduce the size of the landing ellipse and decrease the total integrated heat load, the entry trajectories were biased to have a steep entry flight path angle. The 1U entry vehicle has a 4.5 m diameter parachute with a 1.06 kg mass to enforce the 5 m/s landing requirement.

Table 10: Baseline entry trajectory for 1U cases in spherical atmosphere relative coordinates.

	R (km)	Lon (°E)	Lat (°N)	V (m/s)	γ (°)	Σ (°)
LEO	6503.1	137.29	-22.98	7780	-5	182.9
GTO	6503.1	128.64	-35.92	9964.4	-6.72	57.8

Figure 9.LEO 1U trajectory with stagnation heat rate constraint

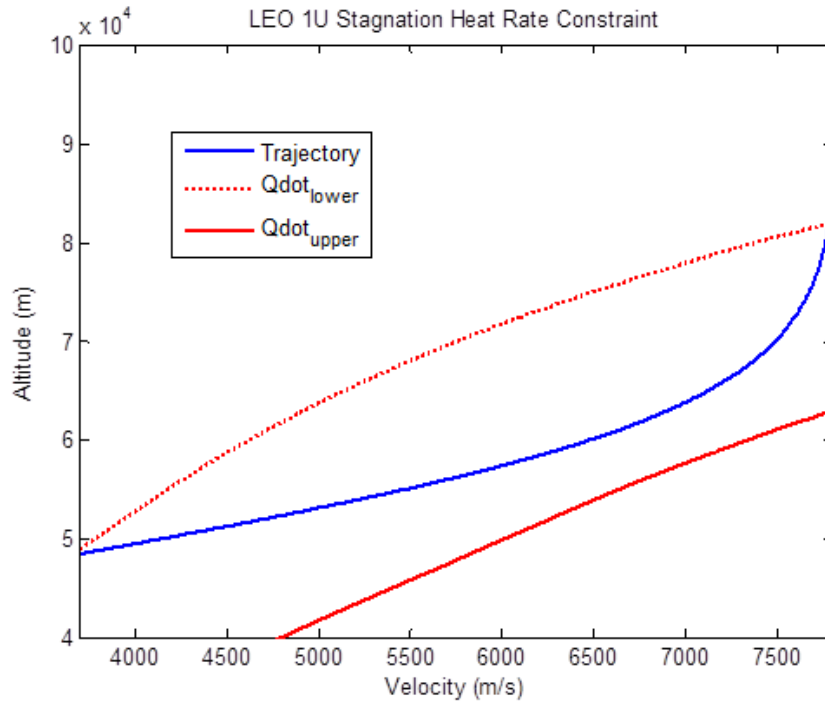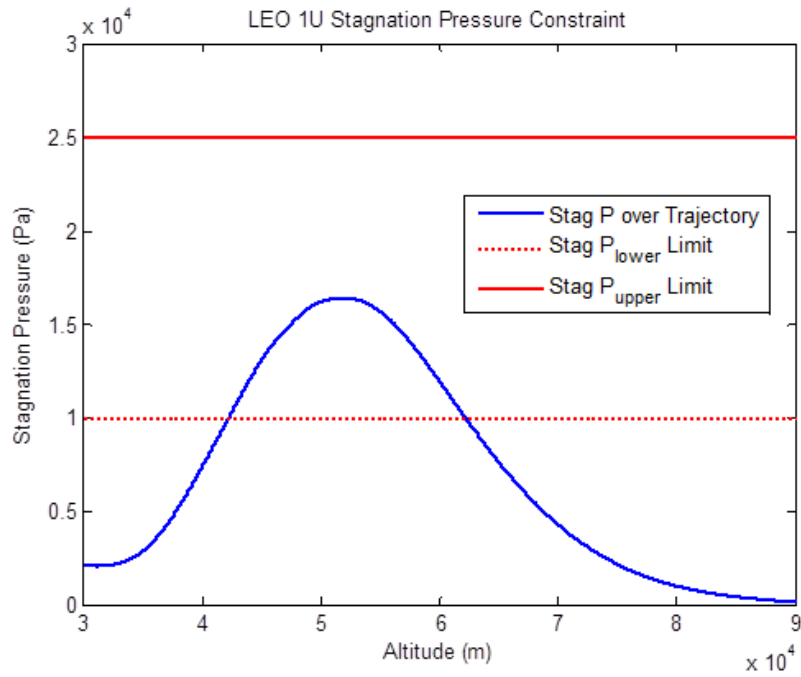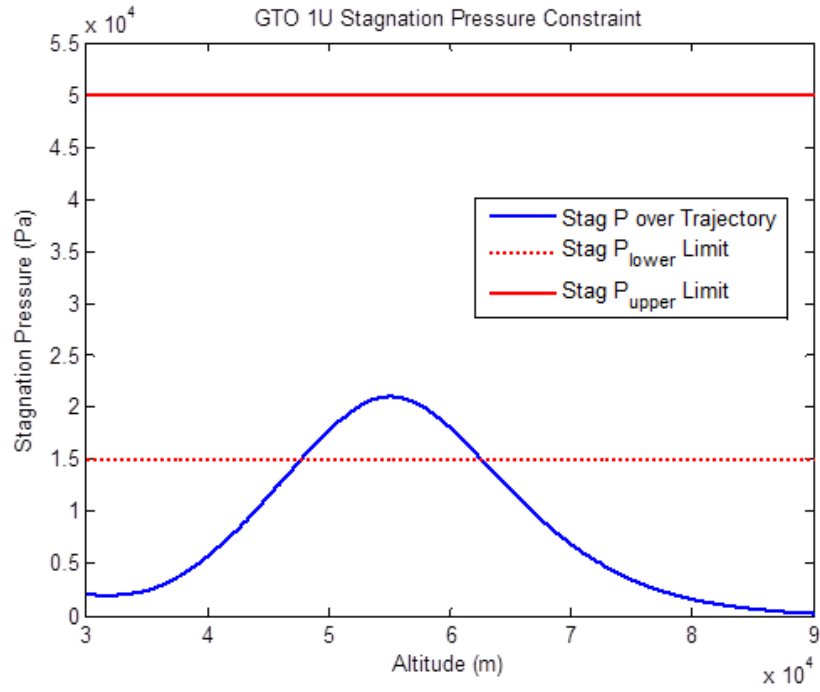**Figure 10.LEO 1U trajectory with stagnation pressure constraints**

Figure 11.GTO 1U trajectory with stagnation pressure constraints.
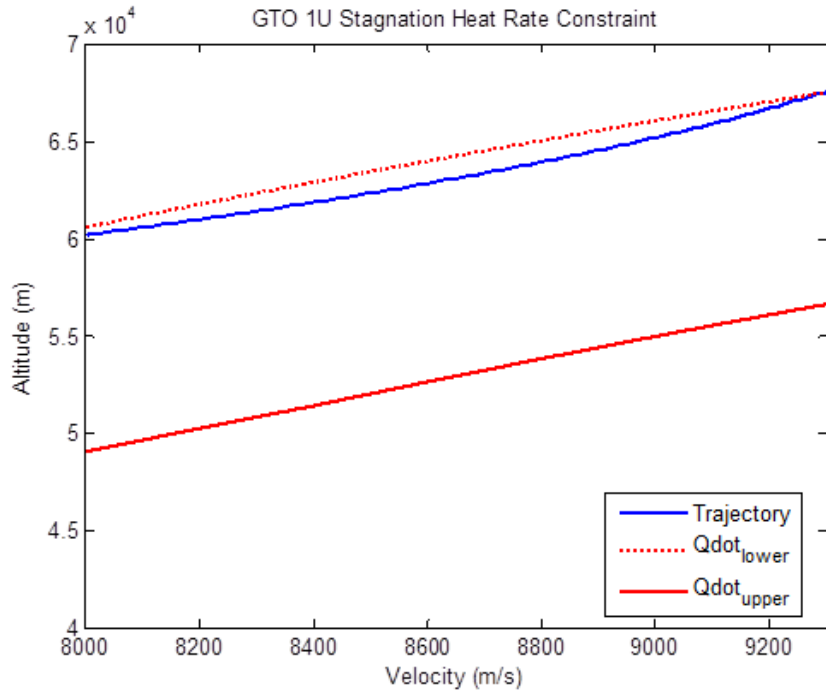

Figure 12.GTO 1U trajectory with stagnation heat rate constraint

For the 2U scenario, nominal entry trajectories were also designed to meet the constraints given in Table 1. The LEO and GTO baseline trajectories are given in Table 11. Figure 13and Figure 16depict the 2x2U LEO and GTO trajectory profiles respectively. Figure 14 and Figure 17 show the maximum acceleration the vehicle experiences over time. The maximum acceleration graphs demonstrates that the 9g, 16g, and 40g loading constraints given in Table 1 are met. Figure 15 and Figure 18 give the stagnation heat rate and dynamic pressure over time. The large increase in dynamic pressure during parachute deployment is a property of the parachute model. The parachute is modeled as an infinite mass which causes a sharp increase in deployment force and dynamic pressure. A higher fidelity parachute model is underdevelopment.

Table 11: Baseline entry trajectory for 2U cases in spherical atmosphere relative coordinates.

	R (km)	Lon (°E)	Lat (°N)	V (m/s)	γ (°)	Σ (°)
LEO	6503.1	137.59	-14.85	7780.5	-5.04	183.0
GTO	6503.1	121.31	-40.89	9964.3	-6.23	57.8

The baseline entry trajectories in Table 10 and Table 11target Woomera, Australia at 31°12′0″S, 136°49′0″E. In order to reach Woomera from the GTO trajectory, a 2.5° inclination change will be performed at apogee during the deorbit burn.
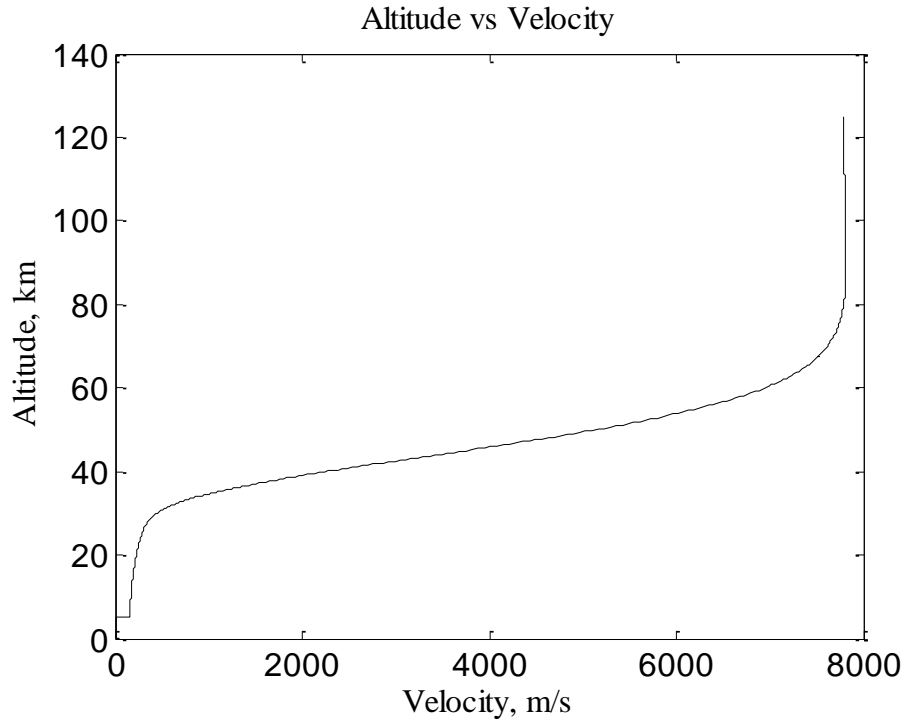

Figure 13. 2x2U LEO trajectory profile.

Figure 14. 2x2U LEO altitude and acceleration vs. time.

Figure 15. 2x2U LEO stagnation point heat rate and dynamic pressure vs. time.

Altitude vs Velocity

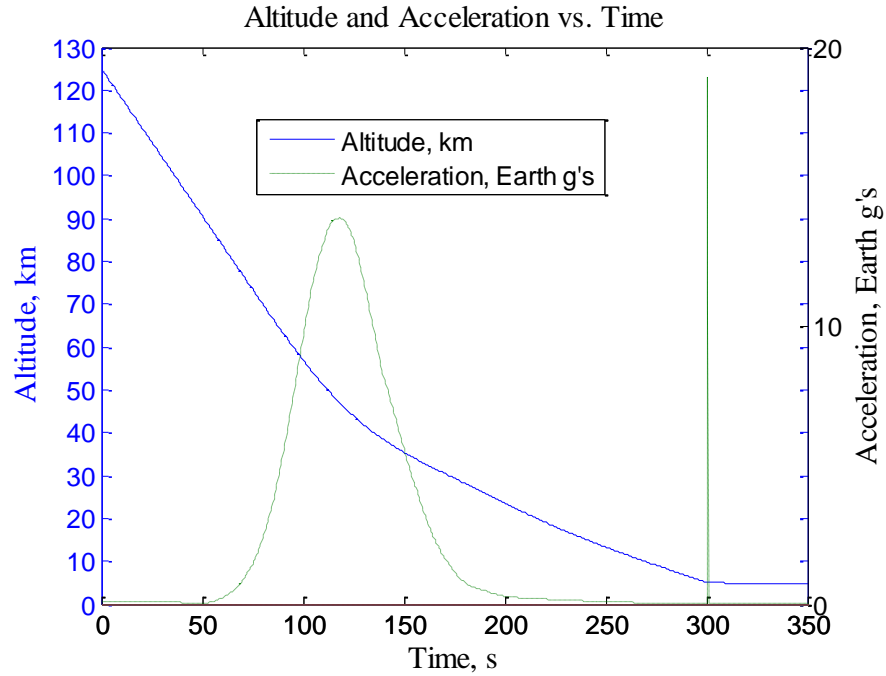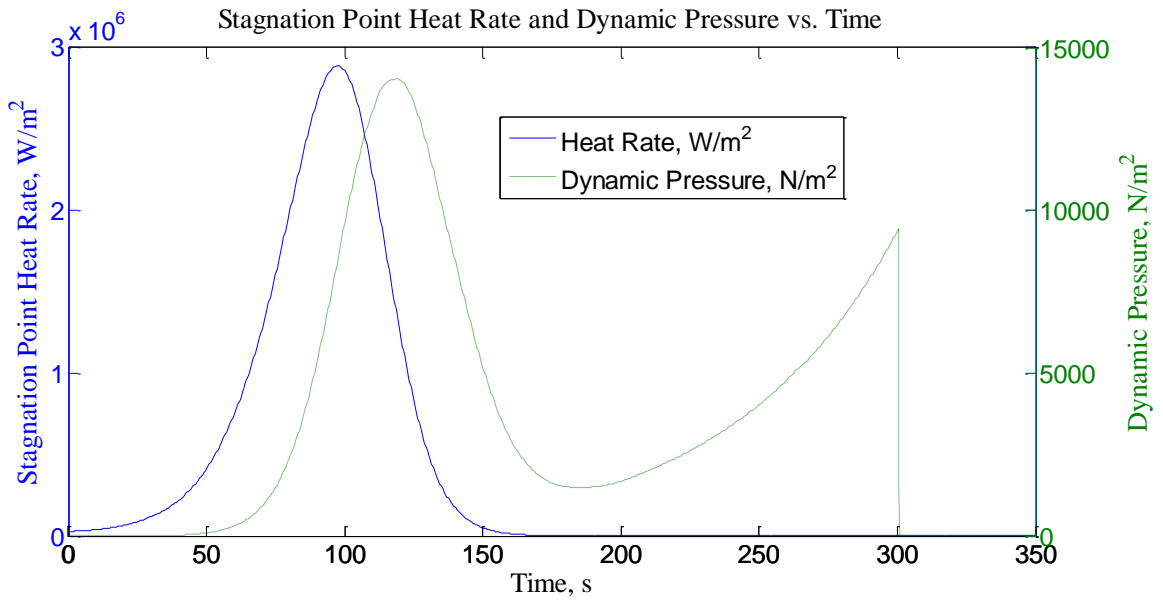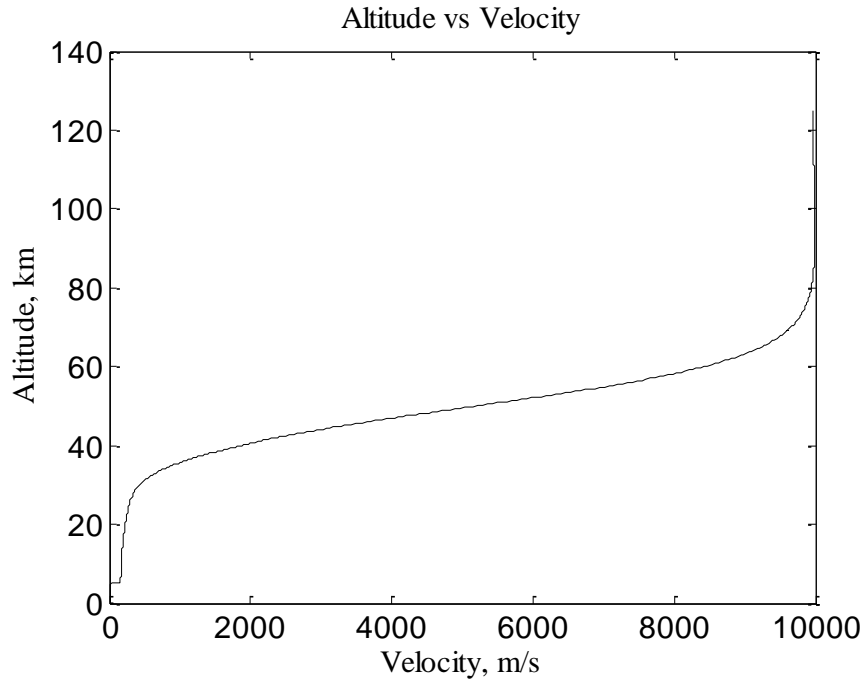**Figure 16.2x2U GTO trajectory profile.**

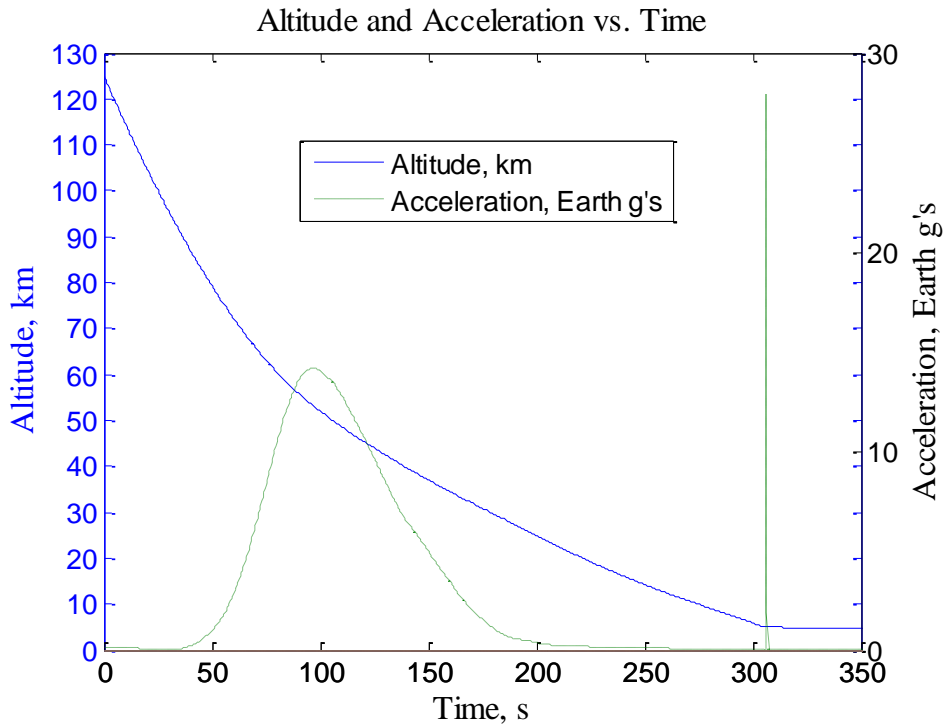## Altitude and Acceleration vs. Time

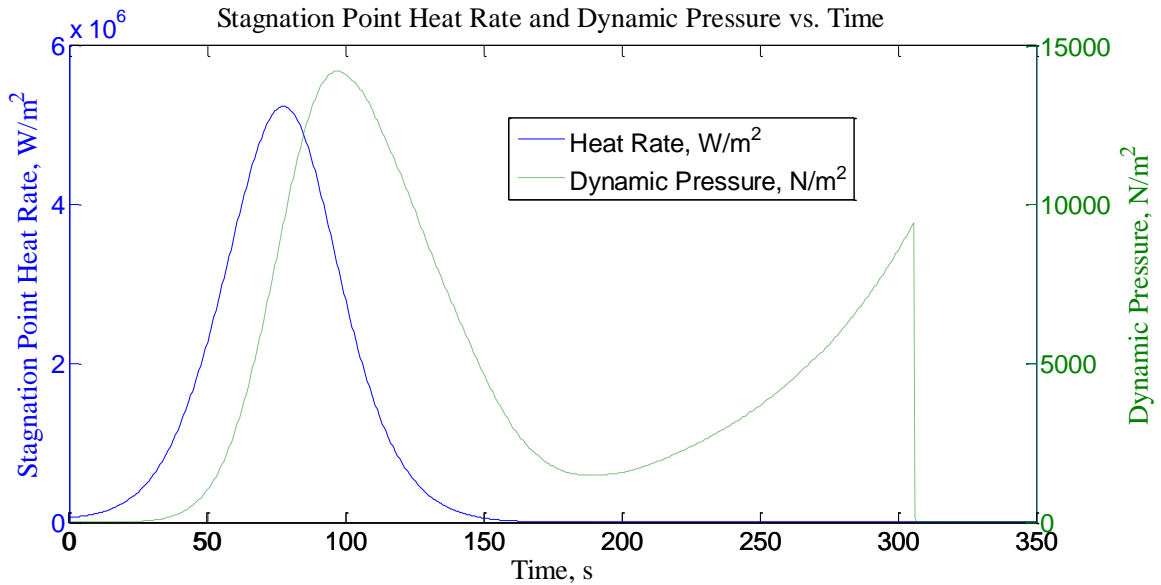**Figure 17.2x2U GTO altitude and acceleration vs. time.**

Figure 18.2x2U GTO stagnation point heat rate and dynamic pressure vs. time.

4.7 Entry Trajectory Simulation

This section describes the simulations used to model the re-entry trajectories from LEO and GTO.

4.7.1 Entry Uncertainties

Entry state, aerodynamic, and atmospheric uncertainties were all modeled in the entry trajectory simulations. The uncertainties used in the 3 DOF and 6 DOF simulations are given in Table 12 and Table 13 respectively. Entry state uncertainties flow down from the deorbit burn simulation and the 3-σ values listed in Table 9. Atmospheric uncertainties were modeled using EarthGRAM (Global Reference Atmospheric Model) to randomly generate tables of 1000 atmospheres. These atmospheres were used in a Monte Carlo simulation and represent the uncertainties in density, temperature, and winds from 0 to 125 km altitude. The aerodynamic dispersions were taken for the Mars Microprobe aerodynamic uncertainties.[11]The 3 DOF model only disperses the drag coefficient aerodynamic uncertainty. The center of gravity offsets in the axial and radial directions, as well as the moment of inertia and initial body rate variations listed in Table 13are taken from the Mars Pathfinder EDL Monte Carlo study1.

Table 12. Uncertainties used in 3 DOF Monte Carlo analysis.

3 DOF Input Variable		Nominal 1U	Nominal 2x2U	Variation	Distribution
Aerodynamic Coefficient	C_D Mach ≥ 10	See Reference [11]		± 3% (3σ)	Normal
	C_D Mach ≤ 5	See Reference [11]		± 10% (3σ)	Normal
Initial Entry State	γ,V,Ψ,θ,φ	See Baseline Trajectories		See entry Table 9	Normal
Atmospheric Uncertainties	Density, Temperature	1976 Standard Atmosphere		EarthGRAM 1000 random atmospheres	--
	Winds	None		EarthGRAM 1000 random atmospheres	--

Table 13.Uncertainties used in 6 DOF Monte Carlo analysis

6 DOF Input Variable		Nominal 1U	Nominal 2x2U	Variation	Distribution
Center of Gravity Offset	Axial (x)	143 mm	245 mm	±1 mm (3σ)	Normal
	Radial (y and z)	0 mm	0 mm	±3 mm (3σ)	Normal
Moment of Inertia	Ixx	0.1 kg-m^2	0.7 kg-m^2	±0.0001 kg-m^2 (1σ)	Normal
	Iyy, Izz	0.08 kg-m^2	0.06 kg-m^2	±0.0001 kg-m^2 (1σ)	Normal
Initial Body Rates	Initial Roll Rate	0 deg/s	0 deg/s	±0.6 deg/s (3σ)	Normal
	Initial yaw and pitch rates	0 deg/s	0 deg/s	±1.1 deg/s (3σ)	Normal
Initial Attitude	Initial angle of attack	0 deg/s	0 deg/s	± 9 deg (3σ)	Normal
Initial Entry State	γ,V,Ψ,θ,φ	See Baseline Trajectories		See Table 9	Normal
Aerodynamic Coefficients	C_A Mach $\geq$ 10	See Reference [11]		± 2% (3σ)	Normal
	C_N Mach $\geq$ 10	See Reference [11]		± 5% (3σ)	Normal
	C_m Mach $\geq$ 10	See Reference [11]		± 0.3% (3σ)	Normal
	C_A Mach $\leq$ 5	See Reference [11]		± 10% (3σ)	Normal
	C_N Mach $\leq$ 5	See Reference [11]		± 10% (3σ)	Normal
	C_m Mach $\leq$ 5	See Reference [11]		± 0.6% (3σ)	Normal
	Parachute C_D	0.66	0.7	± 13% (3σ)	Normal
Atmospheric Uncertainties	Density, Temperature	1976 Standard Atmosphere		EarthGRAM 1000 random atmospheres	--
	Winds	None		EarthGRAM 1000 random atmospheres	--

The center of gravity offset is directly related to the stability of the vehicle. The tolerance give in Table 13 was found through a sensitivity study. The center of gravity was offset incrementally in the radial and axial directions until the vehicle became unstable. During this analysis the, the maximum dispersions 3σ dispersions of the remaining variables were added one at a time to assess their impact on the vehicle's stability. Thus, the 3σ values given in Table give a stable configuration.

The tight ±1 mm center of gravity offset tolerance in the axial direction is a consequence of the X_{CG}/D stability ratio found for the Mars Microprobe vehicle.9 In reality this tolerance only denotes an upper limit. If X_{CG} position is reduced 100 mm the vehicle is still stable.

4.7.2 One variable at a time sensitivities *(The data in this section was generated by Jenny Kelly.)*

After quantifying the entry state uncertainties, each variable shown in Table 14 was varied ±3σ to measure the effect on the rest of the entry state variables. The 3σ variations are taken from the uncertainties in Table 9. The results of this sensitivity study are given in Figure 19 - Figure 234. Results reveal that the entry conditions are most sensitive to changes in the entry vehicle mass, drag coefficient, and entry vehicle diameter. The mass and diameter of the entry vehicle control the ballistic coefficient which is known to drive the entry trajectory. Changing the drag coefficient changes the amount of deceleration the vehicle experiences. Therefore it is expected that changes in drag coefficient have a significant impact on the other entry condition variables.

These trends were used to intelligently manipulate design variables to obtain a converged design that met all the entry requirements.

Table 14. Sensitivity parameters

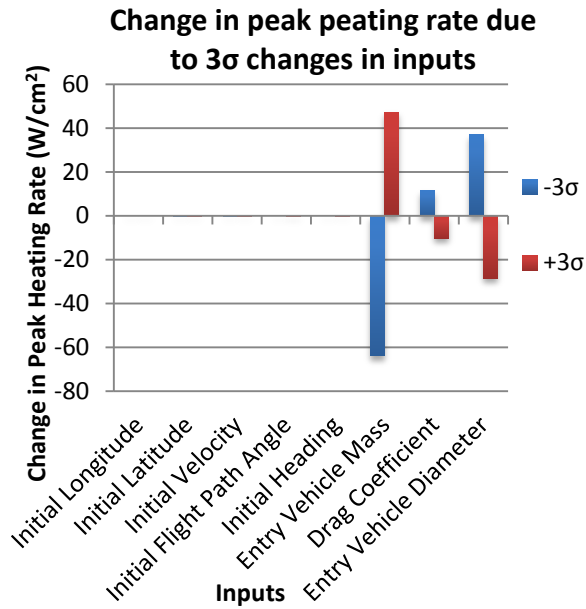| Input	Units	Nominal Value	3σ Changes	
			Backward	Forward
Initial Longitude	deg	-137.65	-0.1663	0.1663
Initial Latitude	deg	-16.65	-0.2401	0.2401
Initial Velocity	m/s	7910.3	-0.3393	0.3393
Initial Flight Path Angle	deg	-2.88	-0.0053	0.0053
Initial Heading	deg	267.1	-0.0181	0.0181
Entry Vehicle Mass	kg	8.74	-4.28	4.28
Drag Coefficient	--	--	-10%	10%
Entry Vehicle Diameter	m	0.4064	-0.06	0.06

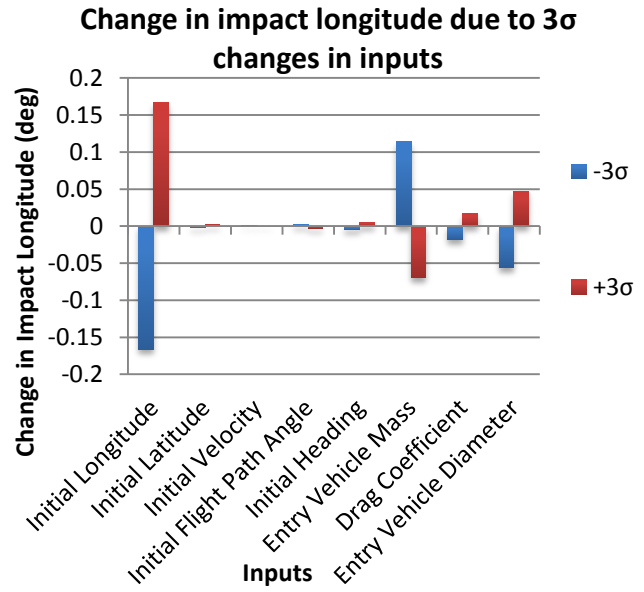**Figure 19.Peak heating rate sensitivities.**

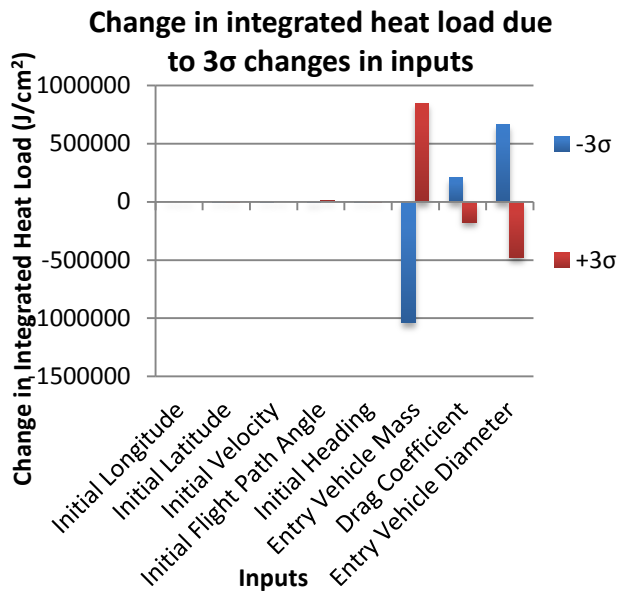**Figure 20.Impact longitude sensitivities.**

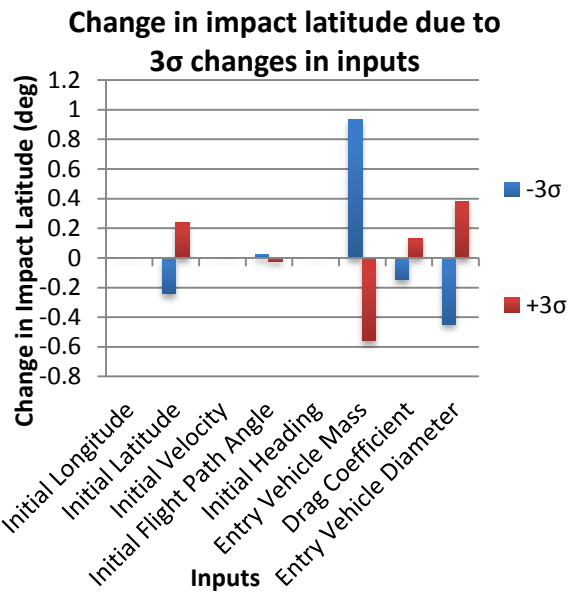**Figure 21.Impact latitude sensitivities.**

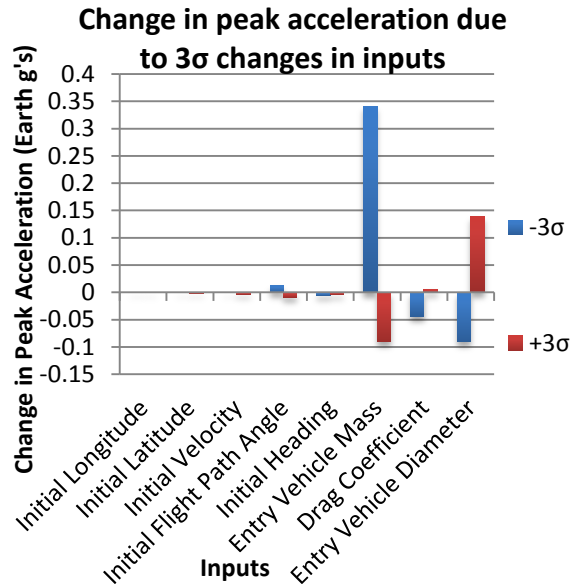**Figure 22.Integrated heat load sensitivities.**

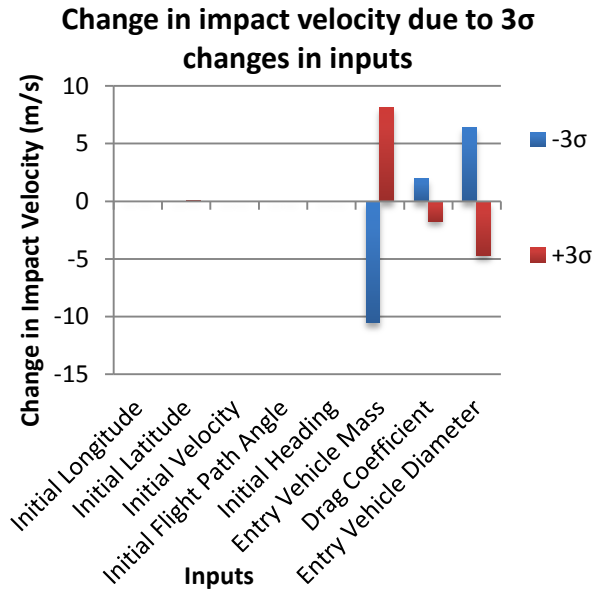**Figure 23.Impact velocity sensitivities.**   **Figure 24.Peak acceleration sensitivities.**

4.7.3 3 DOF Simulation and Monte Carlo Results[3] (*This section was completed with the help of Matt Nehrenz's 3DOF simulation code and Monte Carlo Analysis.*)

In order to predict whether or a not a certain entry vehicle design or entry state meets the constraints on the entry trajectory, a Monte Carlo analysis was performed. Constraints include maximum dimensions on landing ellipse and G-loading. Entry state, aerodynamic, and atmospheric uncertainties are all modeled in the 3 DOF entry trajectory simulations. Entry state uncertainties flow down from the deorbit burn simulation and the 3-sigma values are given in Table 9.Uncertainties on the drag coefficient of the 45° sphere cone are different depending on Mach number, and the values are listed in Table 12.Atmospheric uncertainties were modeled by using EarthGRAM to randomly generate tables of 1000 atmospheres. These atmospheres are cycled through during the Monte Carlo simulation and represent the uncertainties in density, temperature, and winds from 0 to 125 km altitude.

The trajectory simulation is 3 DOF with bank angle modulation; it was written in MATLAB and serves as the primary means of evaluating the 3DOF entry, descent, and landing trajectory for SPORE. In general, bank angle modulation allows a vehicle's lift vector to change orientation, but for this simulation, it is used as a means to incorporate a wind vector from EarthGRAM. The simulation works by solving the equations of motion for a ballistic, non-lifting entry trajectory, and is split into the hypersonic and parachute trajectory.

The hypersonic portion contains calculations for heating statistics and G-loading on the entry vehicle. The Sutton-Graves equation is used to calculate the stagnation point heat flux, and this value is numerically integrated over time to determine the integrated heat load. A G-timer is also used to calculate the times and values corresponding to maximum G-loading cases to ensure constraints are not exceeded and also to serve as a timer to trigger parachute deployment in future simulations. Currently, an altitude trigger is used in the simulation, and once an altitude of 5 km is reached, the parachute is deployed. The altitude of 5 km was chosen as it was approximately between the 3.1 km main

deployment altitude of Stardust and the 10 km main deployment altitude of Hayabusa. At this altitude, the entry vehicle is traveling at a low subsonic speed at a near 90° flight path angle.

In the parachute portion of the trajectory, an instantaneous inflation was modeled to save time during runs. For nominal simulations, a linear inflation profile with time delay for line stretch was chosen for more accurate modeling. Other than the increased drag modeled by the parachute, the equations of motions also included a contribution from winds. By trimming the parachute-vehicle system to the relative wind vector, the wind contributions to the entry vehicle landing dispersions were modeled. Logic is also present in the code to check for the maximum dynamic pressure parachute constraints.

For the Monte Carlo simulations, 250 runs of the trajectory were performed to capture a large enough population and keep the run time short to allow for analysis with other tools. During a collaborative design session, entry vehicle design changes and entry state tweaks resulted in all four cases meeting all constraints. The nominal values settled upon during this session are given in Table 15.

Table 15: 3 DOF Monte Carlo summary

	1U LEO	1U GTO	2x2U LEO	2x2U GTO
Nominal Entry Velocity (m/s)	7780	9964.4	7780.5	9964.3
Nominal Entry Flight Path Angle (°)	-5	-6.71	-5	-6.23
Worst Case Heat Flux (W/cm2)	267.2	514.8	279.6	487.3
Worst Case Integrated Heat Load (J/cm2)	12857	22227	13680	26175
Maximum G's	15.65	20.33	15.98	15.55
Landing Ellipse Downrange (km)	58.5	37.4	53.5	51.48
Landing Ellipse Crossrange (km)	33.5	4.9	31.5	4.51

Next, Figure 25 shows the landing dispersions and 3-sigma ellipses for the 1U LEO and 1U GTO cases.
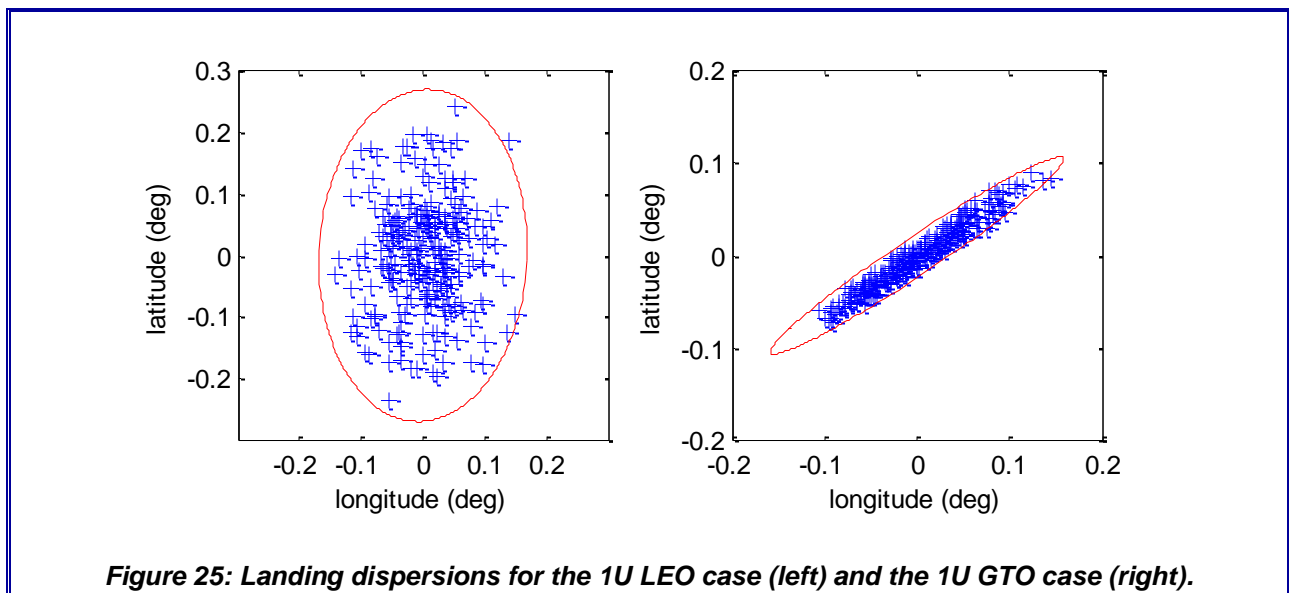

Figure 25: Landing dispersions for the 1U LEO case (left) and the 1U GTO case (right).

Both landing ellipses are well within the constraints. Although the GTO entry flight path angle uncertainty is larger than the LEO case, the GTO landing ellipse is smaller because the nominal flight path angle for GTO is steeper than the LEO case.

The 2U LEO and 2U ISS landing dispersions are displayed in Figure 26.Again, both landing ellipses are of acceptable size and all constraints are met.

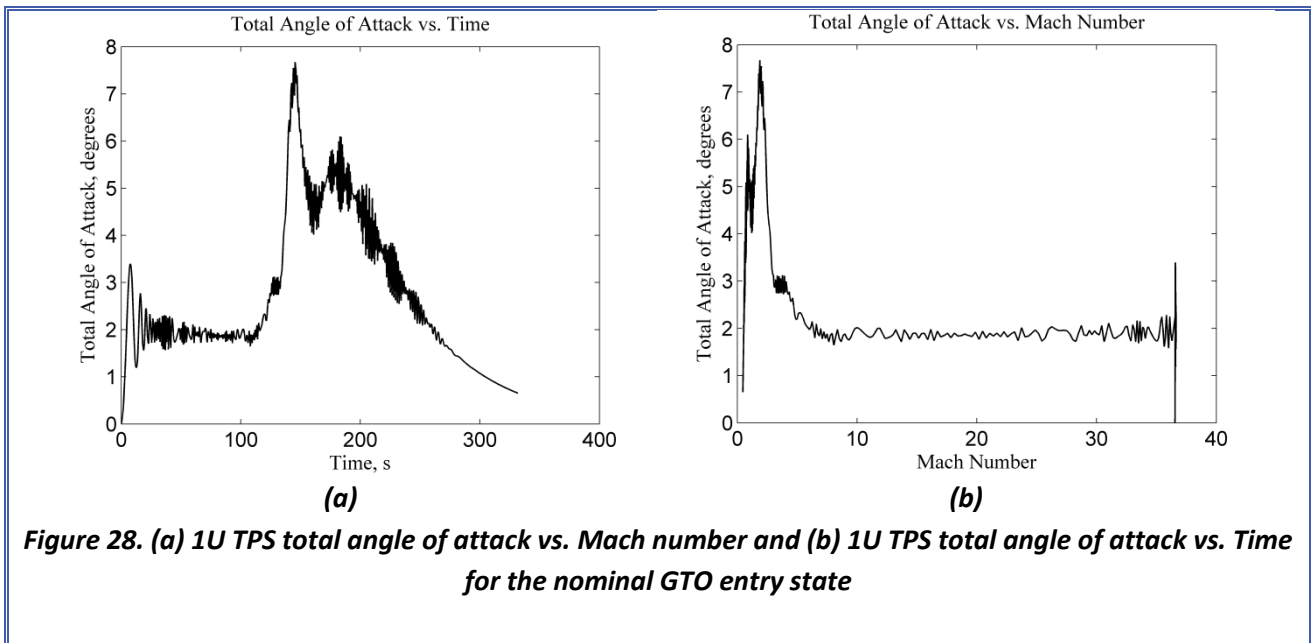***Figure 26: Landing dispersions for the 2x2U LEO case (left) and the 2x2UU GTO case (right)***
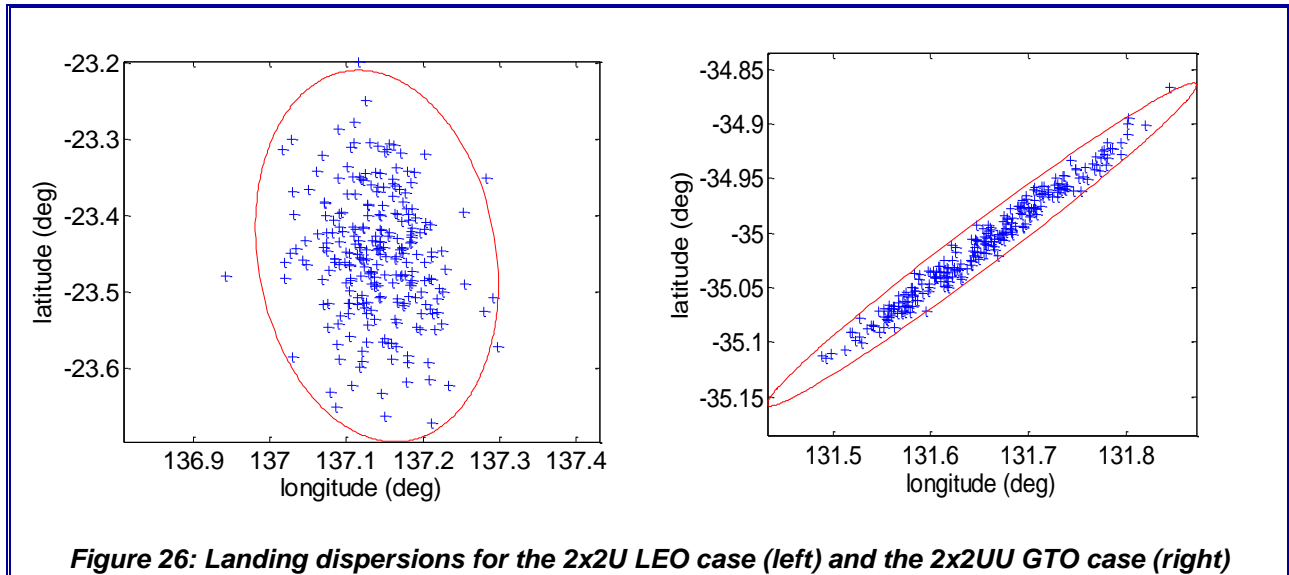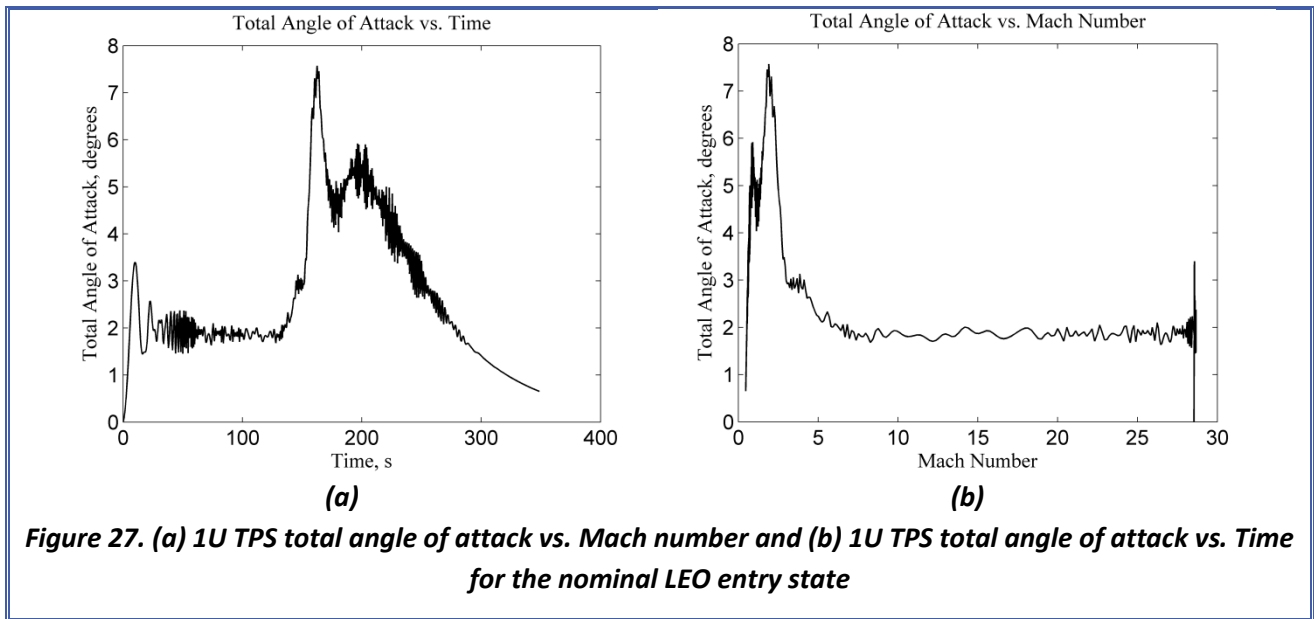
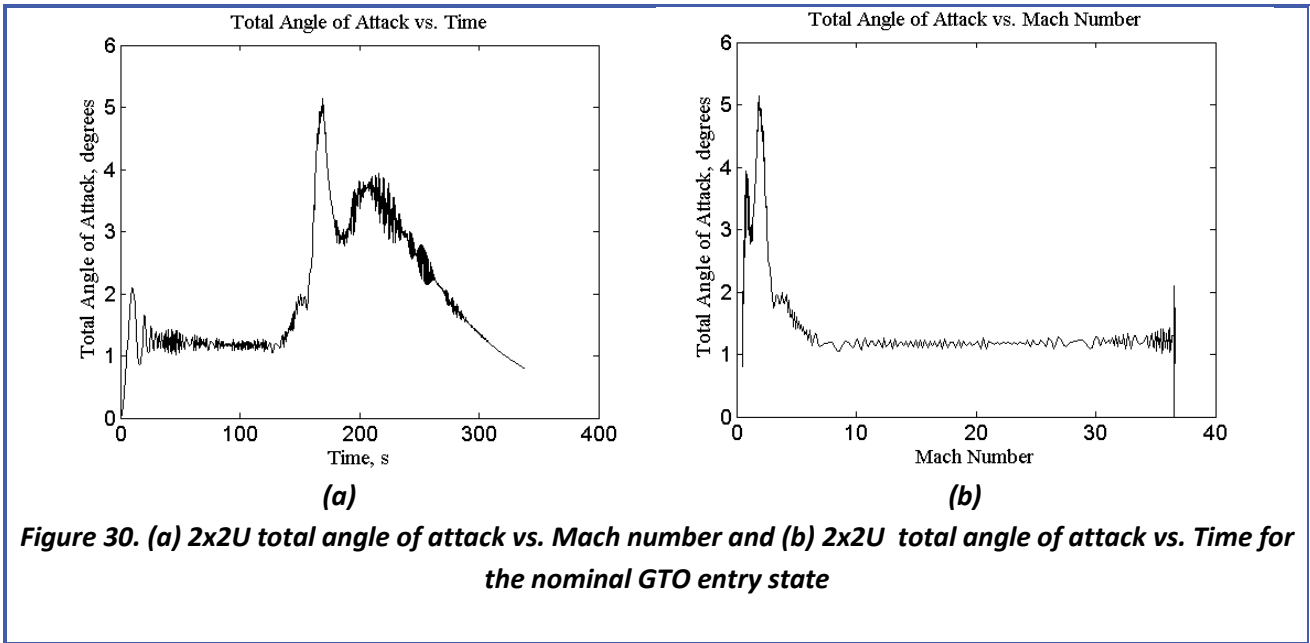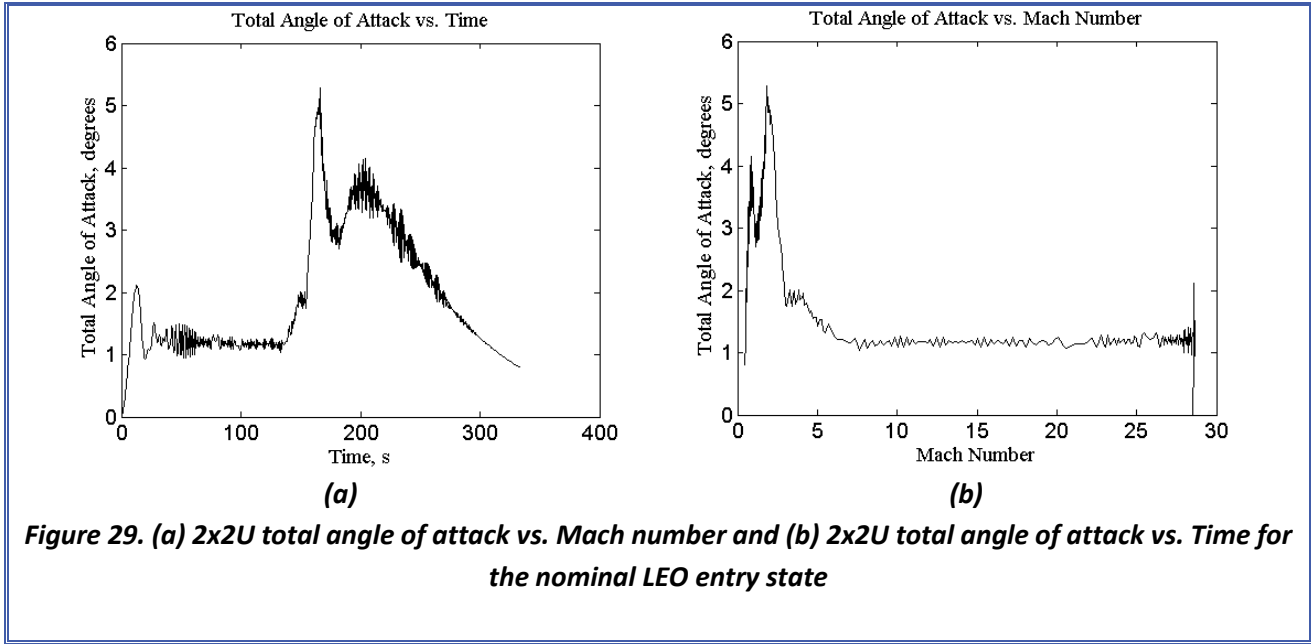### 4.7.4   6 DOF Stability Analysis

SPORE adopted the Mars Microprobe 45° sphere cone geometry designed by NASA Langley to simplify the re-entry architecture and ensure passive stability throughout hypersonic, supersonic, and subsonic re-entry phases[13]. Due to packaging constraints, the center of gravity requirement that ensures stability cannot be met. A 6 DOF stability analysis has been completed to assess stability with the new cg location.

The 6DOF model uses the Mars Microprobe aerodynamic database found in the literature[13] and 1976 standard atmospheric tables. To simulate a passive entry vehicle, no steering was applied to the model and the vehicle was initialized for ballistic entry. This model does not include a parachute so that dynamic stability can be assessed throughout the entire trajectory. Atmospheric winds were not included in this model.

The vehicle is considered dynamically stable if the total angle of attack remains under five degrees1. Results show that the 1U vehicle crosses this threshold. However, this constraint will be reassessed in future analysis to align with the capabilities of the parachute. The 2x2U entry vehicles remain stable throughout the entire entry trajectory. There is an increase in total angle of attack as the vehicle approaches the transonic regime, but the oscillations are damped out over time. The model has the option to spin the vehicle to increase dynamic stability, but results show this is not necessary. The 1U TPS total angle of attack is plotted in Figure 27 and Figure 28 for the LEO and GTO entry states,

respectively. Figure 29 and Figure 30 present the total angle of attack trends for the nominal 2x2U LEO and GTO entry trajectories, respectively.

Figure 27. (a) 1U TPS total angle of attack vs. Mach number and (b) 1U TPS total angle of attack vs. Time for the nominal LEO entry state

Figure 28. (a) 1U TPS total angle of attack vs. Mach number and (b) 1U TPS total angle of attack vs. Time for the nominal GTO entry state

Figure 29. (a) 2x2U total angle of attack vs. Mach number and (b) 2x2U total angle of attack vs. Time for the nominal LEO entry state

Figure 30. (a) 2x2U total angle of attack vs. Mach number and (b) 2x2U total angle of attack vs. Time for the nominal GTO entry state

4.7.5 6 DOF Monte Carlo Analysis

Atmospheric winds generated from EarthGRAM and a 3 DOF parachute model were added to the POST II model used for the stability analysis. The dispersions given in Table 13 were used to complete a 250 run Monte Carlo analysis on the higher fidelity model. The results are given below. As seen in Figure 31, Figure 33, Figure 35, and Figure 37 all cases are stable since the total angle of attack remains bounded. These figures also indicate relatively low impact velocities. However a more detailed analysis is needed

to ensure these velocities do not violate the 40 g impact constraint. None of the cases violated the 9g and 16g constraints. The landing ellipse as well as the parachute deployment Mach number vs. dynamic pressure are given in Figure 32, Figure 34, Figure 36, and Figure 38. Results show that all parachute deployments remain subsonic and do not violate the landing ellipse constraint.

Figure 31. 1U LEO maximum total angle of attack (left) and impact velocity (right).

Figure 32. 1U LEO landing ellipse (left) and Mach number vs. dynamic pressure at parachute deployment (right).The was parachute deployed at 5km for all cases.
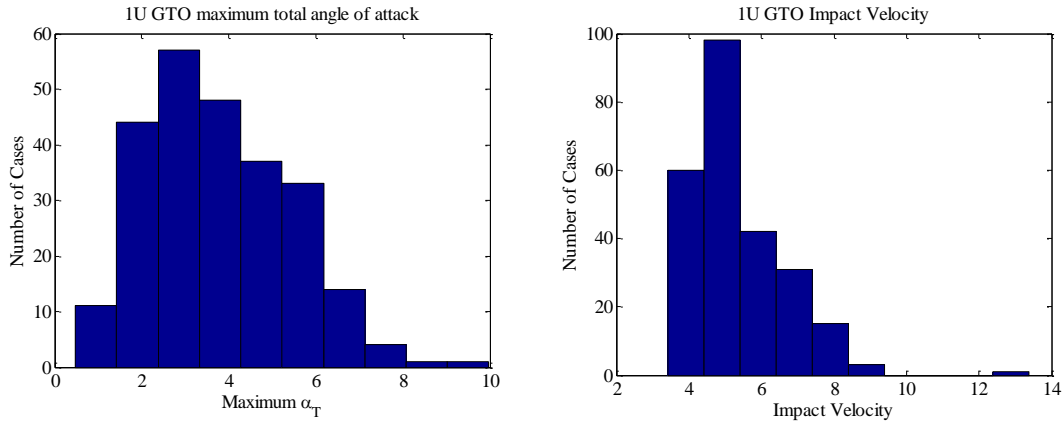
Figure 33. 1U GTO maximum total angle of attack (left) and impact velocity (right).
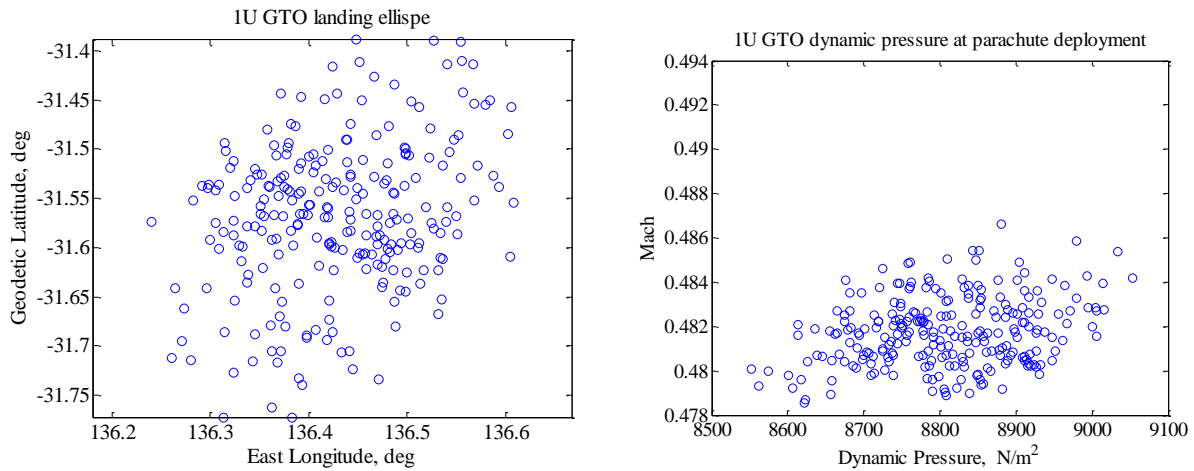
Figure 34. 1U GTO landing ellipse (left) and Mach number vs. dynamic pressure at parachute deployment (right).The was parachute deployed at 5km for all cases.
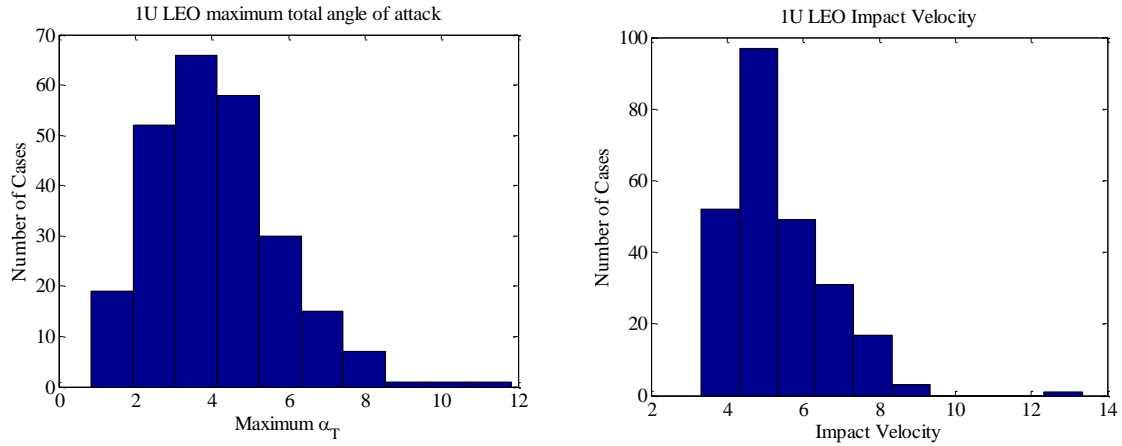

Figure 35. 2x2U LEO maximum total angle of attack (left) and impact velocity (right).

Figure 36. 2x2U LEO landing ellipse (left) and Mach number vs. dynamic pressure at parachute deployment (right).The was parachute deployed at 5km for all cases.

Figure 37. 2x2U GTO maximum total angle of attack (left) and impact velocity (right).
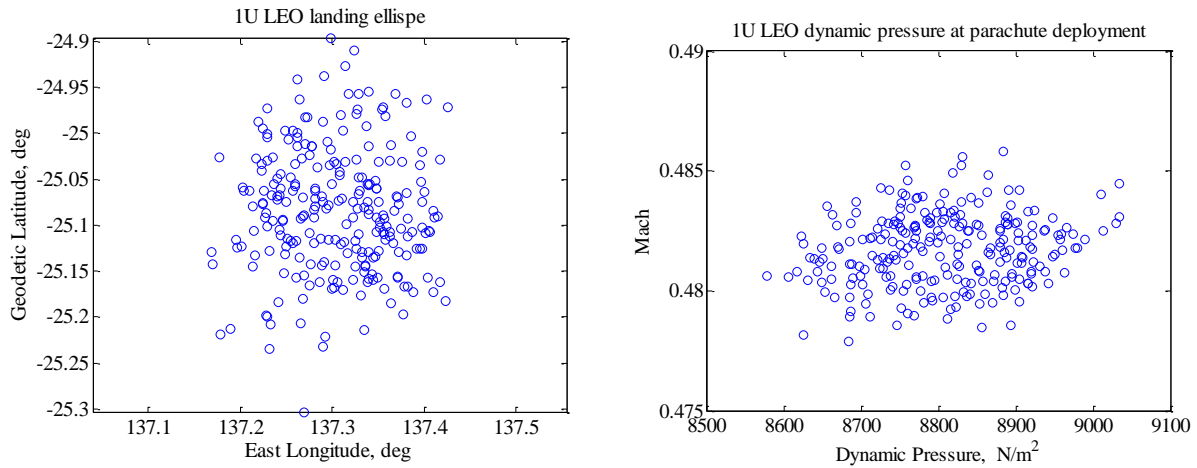

Figure 38. 2x2U GTO landing ellipse (left) and Mach number vs. dynamic pressure at parachute deployment (right).The was parachute deployed at 5km for all cases.
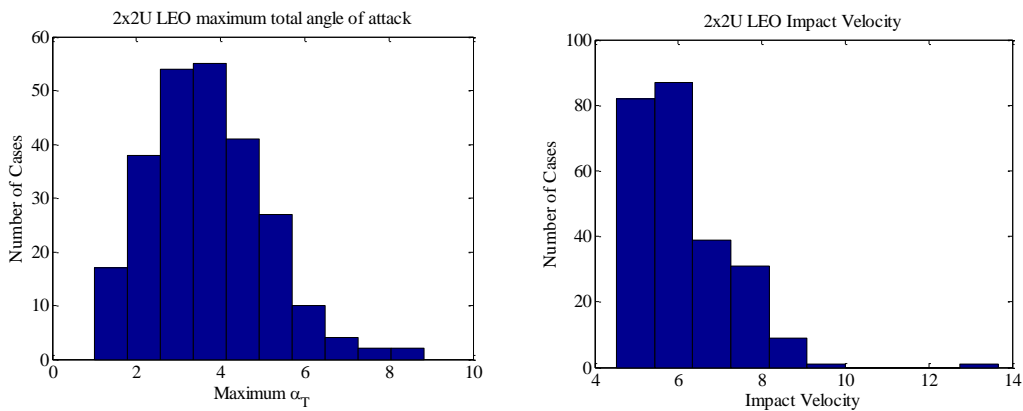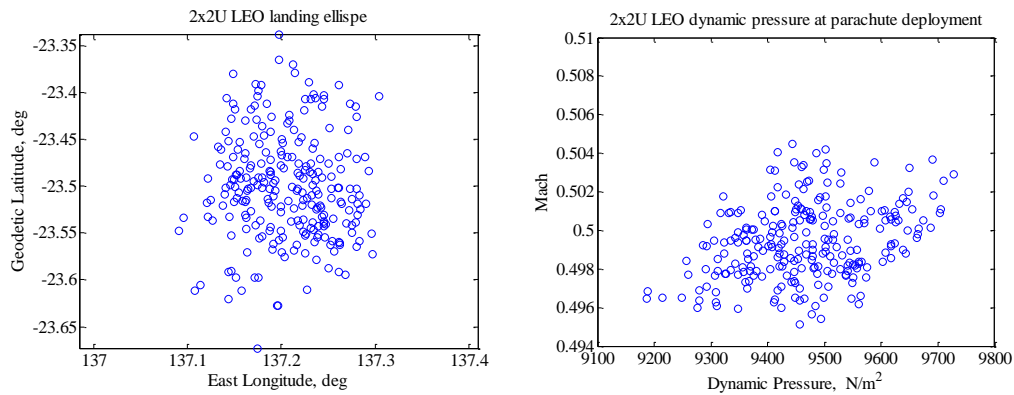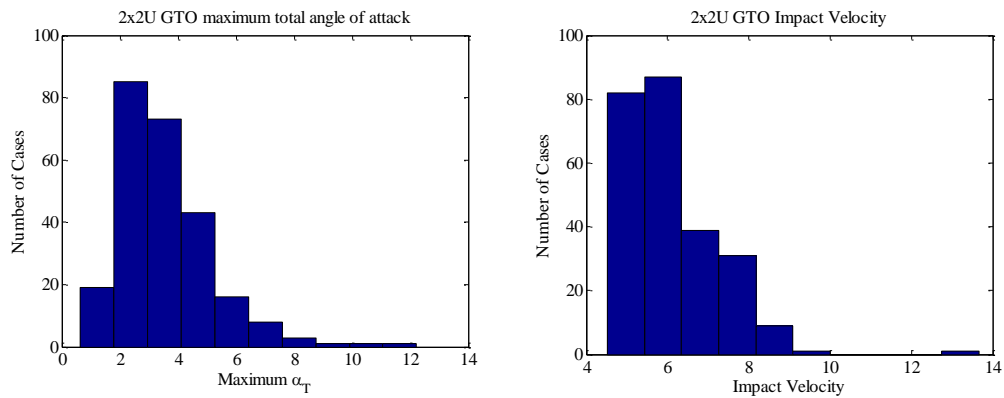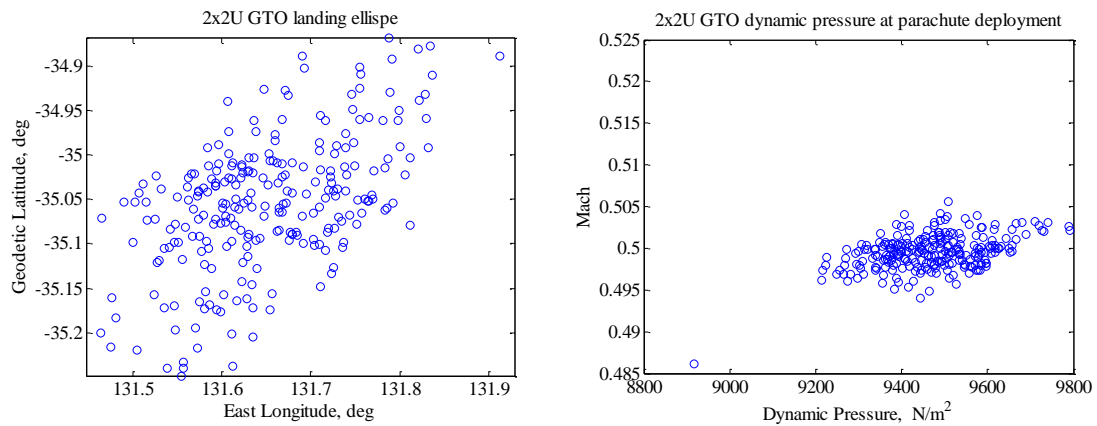
4.8 Parachute Selection

To keep the payload intact, the 1U vehicle must touchdown with an impact velocity below 5 m/s. The 1U vehicle uses a cross parachute manufactured by Pioneer Aerospace for use on 16 kg flares. The parachute is capable of meeting the 5 m/s requirement for vehicles less than 18 kg. A mortar for this parachute consists of a gas generator with electrical ignition, which will push up a sabot and eject the packaged parachute from the top of the backshell. A backshell cap, held in place by shear pins, will pop off when pressure becomes too great and release the parachute. The specifications fpr the 1U parachute are provided in Table 16.

Table 16.1U parachute specifications.

Parachute type	C_D	A (m^2)	D_0 (m)	Mass (kg)
Cross	0.66	15.904	4.5	1.06

To ensure survival of the biological and material science payloads, the 2x2U vehicle must not exceed 40g's during impact and parachute deployment. Discussions with Pioneer Aerospace are currently underway to find a parachute and mortar system that meets the 2x2U requirements, but a preliminary parachute model was developed to ensure all the entry requirements are met.

Meyer's theory was used to determine the terminal velocity required to meet the 40 g impact limit on UTTR soil[10]. NASA Langley performed gantry tests to characterize the acceleration and penetration of a small spacecraft as it impacts UTTR soil. The tests were completed using 0.21 m diameter hemispherical penetrometer at impact speeds between 5-10 m/s. As depicted in
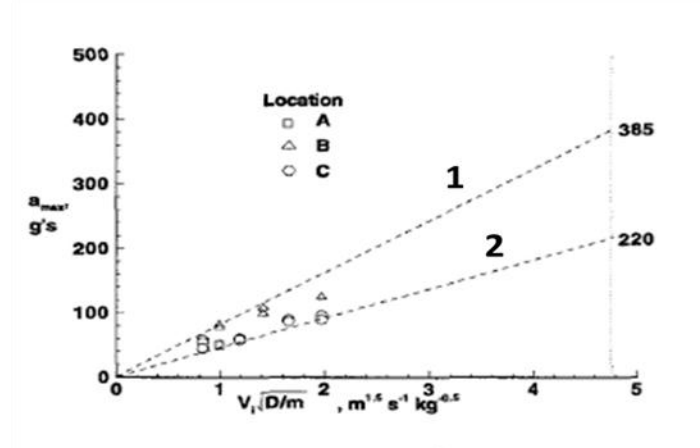

Figure 39, the data revealed that maximum acceleration varies linearly with $V_i\sqrt{D/m}\,V_i\sqrt{D/m}$ where D is the diameter, m is the impact mass, and V_i is the impact velocity.
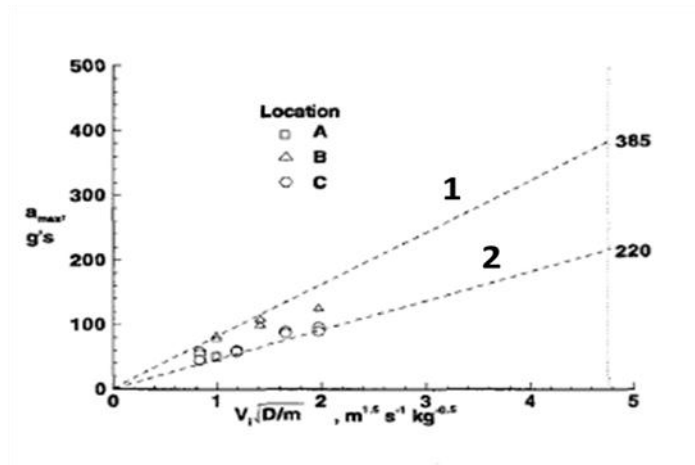
Figure 39: Depicts Meyer's Theory[10].

With a 40g maximum acceleration limit and vehicle mass of 32.3 kg, the terminal velocity is 5 m/s. This terminal velocity was used to find the parachute C_DA using Equation 35. For Equation 35, density was found to be 1.08 kg/m^3 at UTTR elevation using standard atmosphere tables.

$$C_DA = \frac{mg_E}{\frac{1}{2}\rho V_t^2}$$ (35)

The area of the parachute is found by dividing C_DA by the drag coefficient of the parachute. The Tri-Conical, Ringsail, and Cross parachutes were compared due to their high drag coefficients and heritage. Table 17 compares the mass, volume, and deployment load for each parachute[16]. The values are for the 2x2U vehicle.

Table 17. Summary of parachute parameters used for comparison. Green indicates selected parachute.

Parachute type	C_D	A (m^2)	D_0 (m)	Mass (kg)	Volume (m^3)	Deployment Load (g's)
Tri-Conical	0.7	33.79	6.56	2.16	2.70E-03	9.09
Ringsail	0.75	31.54	6.34	2.03	2.54E-03	5.55
Cross	0.6	39.42	7.08	2.35	2.93E-03	5.55

The mass of each parachute was estimated using the TWK method outlined in Reference 16. The following equation gives the formula used to estimate the mass. Table 18 defines the variables in this equation and gives the values used for each parachute. Most of the variables remain the same between parachutes. Therefore parachute area is the principal driver for parachute mass. Due to its low mass and high C_D, the Ringsail parachute was chosen for the 2x2U vehicle.

$$ParachuteMass = S_0 w_c + \frac{D_0}{2} N_G w_{RT} \frac{F_{RT}}{1000} + N_{SL} L_S w_{SL} \frac{F_{SL}}{1000}$$ (36)

Table 18. Summary of parameters used to calculate parachute mass. Green indicates selected parachute.

Symbol	Units	Definition	Tri-Conical	Ringsail	Cross
W_C	lb/ft^2	Specific canopy height	1.15E-02	1.15E-02	1.15E-02
N_G	--	Number of gores	10.00	10.00	1.00
w_{RT}	lb/ft/1000-lb	Specific canopy weight	3.50E-03	3.50E-03	3.50E-03
F_{RT}	lb	Strength of radial tape	855.00	855.00	855.00
N_{SL}	--	Number of suspension lines	10.00	10.00	10.00
L_S	ft	Length of suspension lines	8.76	8.76	8.76
w_{SL}	lb/ft/1000-lb	Specific weight of suspension lines	3.50E-03	3.50E-03	3.50E-03
F_{SL}	lb	Strength of suspension lines	855.00	855.00	855.00
S_0	ft^2	Parachute Area	363.69	339.44	424.30
D_0	ft	Parachute Diameter	21.52	20.79	23.24

A first order estimate of the parachute deployment force was calculated using a finite mass estimation in the following equation[16].

$$\text{Parachute Deployent Force} = (C_D A) q C_x X_1 \qquad (37)$$

In this equation, X_1 represents the opening-force-reduction factor and ranges from 0 to 1 based on canopy loading. Since the canopy loading is low ($\frac{W}{C_D A} = 1.37$), this factor was set to 0.2. The opening force coefficient at infinite mass (C_x) comes from parachute data recorded in Table 19[16]. The parachute deployment force will be updated as higher fidelity parachute models are developed.

Table 19. Opening force coefficients at infinite mass. Green indicates selected parachute.

	Tri-Conical	Ringsail	Cross
C_X	1.8	1.1	1.1

It was assumed that the parachute deploys at Mach 0.8. Using a 3DOF trajectory code the deployment velocity was calculated to be 173 m/s. From these values, the resulting dynamic pressure (q) is 338.2 Pa (the density of the atmosphere is 0.0226 kg/m^3 at deployment condition). To meet the biological and material science payload requirements, the deployment load must stay below 40g. As seen in Table 17, this deployment loading remains within the limits. Parachute loading increases as the deployment altitude decreases due to an increase in atmospheric drag. Techniques like reefing can be used to reduce parachute loading, but preliminary results show that is not necessary.

To avoid supersonic and transonic instabilities, it was decided that the parachute for the 1U and 2x2U vehicles shall be deployed subsonically (below Mach 0.8). A deployment altitude of 5 km was chosen as it falls between the 3.1 km main deployment altitude of Stardust and 10 km main deployment altitude

of the Hayabusa spacecraft8. At this altitude, the entry vehicle is traveling at a low subsonic speed at a near 90° flight path angle. In the future, a G-switch will be utilized to initiate parachute deployment at the desired deceleration level during atmospheric entry. The current Monte Carlo analysis was performed assuming an altitude trigger, but will be updated later to include a G-switch.

4.9   Parachute Model

A 3DOF parachute model was added to the 3 DOF and 6 DOF simulations. In the 3 DOF simulation, the parachute deployment occurs at an altitude of 5 km, but in the future will be modeled as a G-switch. Two types of inflation were modeled. For the Monte Carlo simulations, an instantaneous inflation was modeled to save on run time. For the nominal simulations, a linear inflation profile was assumed using Knacke's[3] inflation time relationship. Atmospheric wind contributions to the entry vehicle landing dispersions were modeled, assuming the parachute-vehicle system trimmed to the relative wind vector.

In the POST model, the parachute was modeled as an increase in drag force according to Equation 38.

$$C_D = \frac{C_{D_{body}}A_{ref_{body}} + C_{D_{parachute}}A_{ref_{parachute}}}{A_{ref_{body}}} \tag{38}$$

To save computation time, the inflation rate of the parachute was not modeled. This explains the large maximum accelerations seen in Figure 41 and Figure 41. The loads in Figure 40 and Figure 41 do not indicate a failure to meet the payload requirements. A higher fidelity parachute model that includes inflation rate is under development. The higher fidelity model will be used to ensure the vehicle meets the 40g acceleration limit imposed by the payload constraints. After the parachute deploys, the vehicle is given a guidance algorithm that trims the vehicle based on atmospheric relative aerodynamic angles. The parachute is deployed at 5km,but in the future will be modeled as a G-switch.
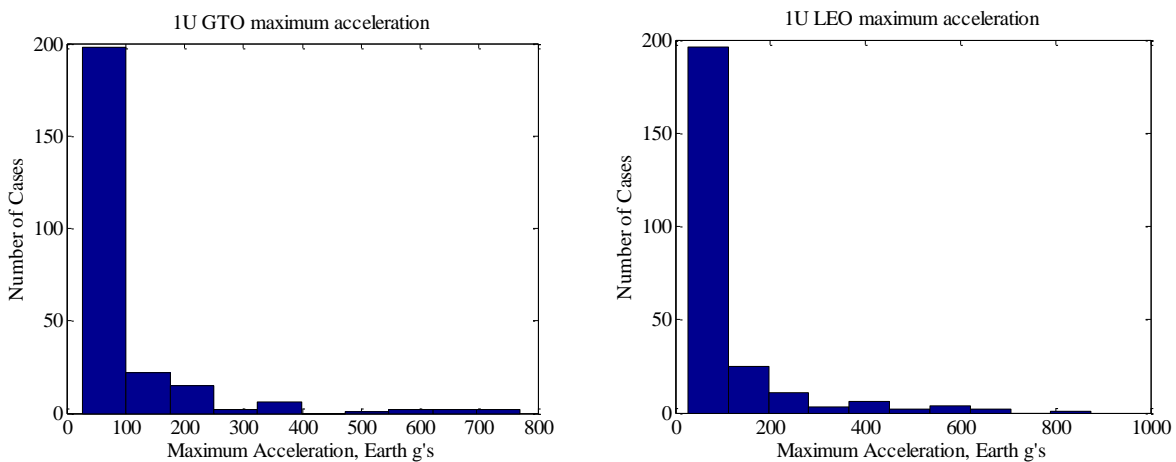

Figure 40. 1U GTO (left) and LEO (right) maximum accelerations. These will be reduced with a higher fidelity parachute model that models parachute inflation rate.
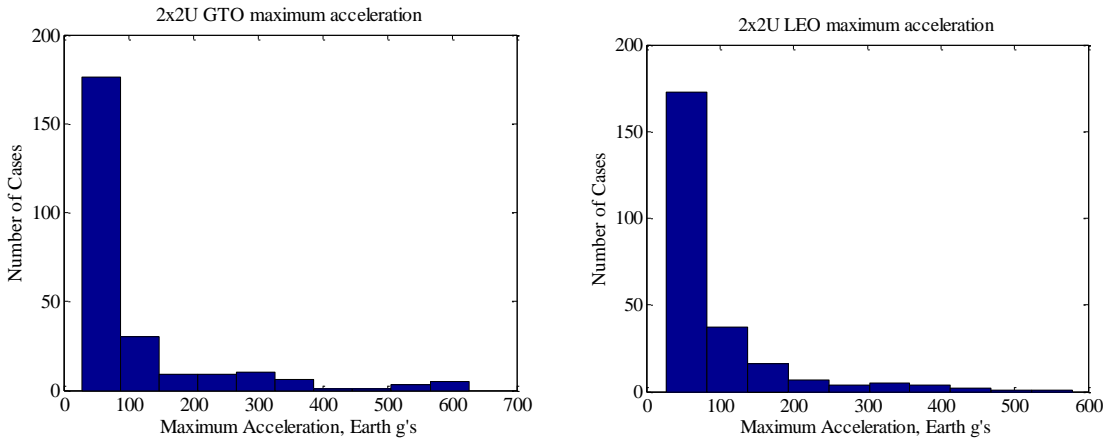
Figure 41. 2x2U GTO (left) and LEO (right) maximum accelerations. These will be reduced with a higher fidelity parachute model that models parachute inflation rate.

4.10 TPS Sizing

PICA was chosen as the forebody TPS material, because of its need for characterization at off-nominal heat fluxes. This makes it a good candidate for TPS testbed missions. The Georgia Tech Planetary Entry Systems Synthesis Tool (PESST) was used to size the TPS material for the 2x2U vehicle[14]. Inputs into PESST include atmospheric relative entry state as well as vehicle mass and geometry[14]. Table 20 gives the TPS thickness for the 2x2U vehicle.

Table 20.TPS forebody thickness.

PICA Forebody Thickness (cm)		
	LEO	GTO
2x2U Vehicle	7.2917	8.4121

The 1U mass and size were not in the scope of the PESST design space. Therefore an accurate TPS sizing could not be calculated from PESST. A TPS forebody thickness of 0.03175 m was assumed for the 1U vehicle. This number will be updated once higher fidelity TPS sizing tools are made available.

4.11 Thermal Soak-back Analysis[3](*This section was updated from the AIAA ASM paper with the help of Jessica Juneau).*

In order to verify that the payload does not exceed the maximum allowable operational temperature during re-entry, a thermal soak-back analysis was performed using FIAT (Fully Implicit Ablation and Thermal Response) program. For this analysis, the worst-case heating trajectories from the 3DOF Monte Carlo simulation were used. The stagnation point convective heating was approximated using the Sutton-Graves relationship, while the radiative heating was approximated using the Martin relationship for Earth entry. The "assigned surface temperature history" option was used in FIAT for the re-entry

segment, while the "cool-down" option was used for a 10,000 second cool down period. The surface temperature was approximated assuming that the re-radiated heat flux is equivalent to the convective and radiative heating, as shown in Equation 39.

$$T_{surf} = \left(\frac{q_{rerad}}{\varepsilon\sigma}\right)^{1/4} \approx \left(\frac{q_{conv} + q_{rad}}{\varepsilon\sigma}\right)^{1/4}$$

(39)

The surface pressures were estimated using normal shock relationships at the vehicle nose, using the freestream density and vehicle Mach number. A plot of the total stagnation point heat flux for the worst case heating trajectories, along with the calculated surface temperatures and pressures are shown in
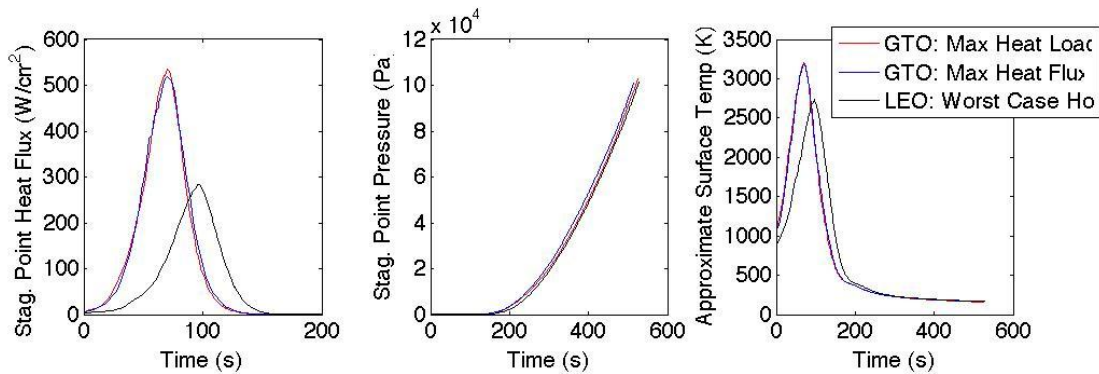

Figure 42.1U worst case heating trajectories: (a) total stagnation point heat flux, (b) surface pressure, and (c) surface temperature.
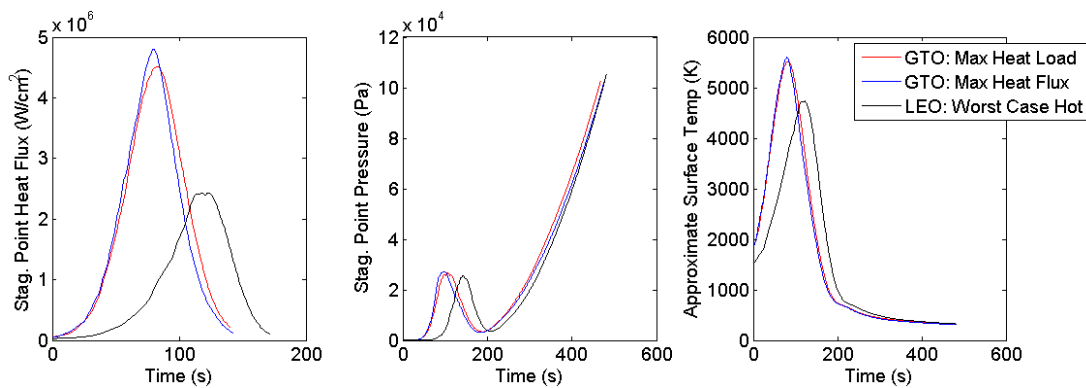

Figure 43.2x2U worst case heating trajectories: (a) total stagnation point heat flux, (b) surface pressure, and (c) surface temperature.

Figure 42and Figure 43for the 1U and 2x2U vehicle respectively. As one can see, the worst case surface temperatures correspond to the GTO return trajectory with the worst case heat flux. Therefore, this assigned temperature and pressure profile were used for the 1-D FIAT heat soak back analysis and heat sink thickness optimization.

The material stack-up used is that described in Section IV: PICA, RTV-560V, Al-6061 forebody structure, Al-6061 heat sink material, radiative gap (air), and the electronics boxes (Al-6061). For the 1U

worst case heating trajectory from GTO, the optimized heat sink thickness was determined to be 41.2 mm. For the 2x2U design, the optimized heat sink thickness for the GTO case was 74.4 mm.

The temperature profiles at the base of each of the layers in the material stack-up are shown in Figure 44and Figure 45 for the 1U and 2x2U vehicles respectively. As one can see the base of the electronics boxes or payload is maintained below the 50°C constraint for the 1U vehicle and 25°C for the 2x2U vehicle.
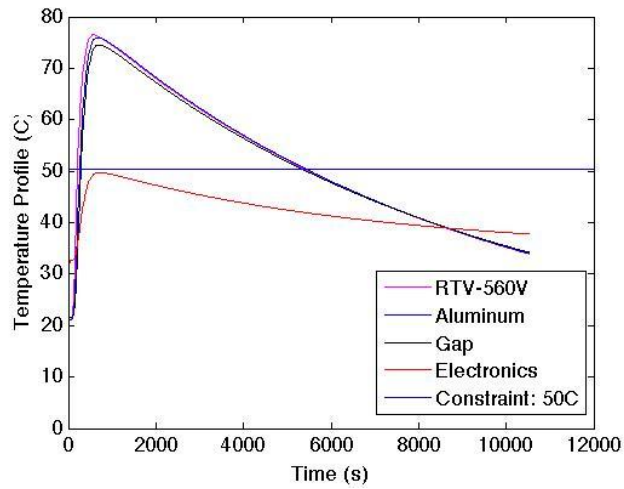

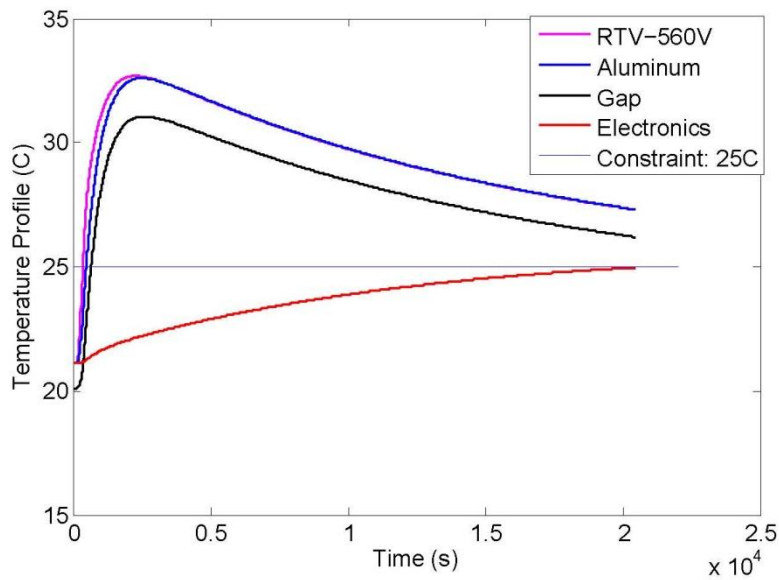*Figure 44.1U temperature profiles for the worst case heating trajectory.*

Figure 45. 2x2U temperature profiles for the worst case heating trajectory.

4.12 Landing and Recovery Procedures

There is not an established landing and recovery procedure for small re-entry probes. The heat sink material is theoretically sized to allow for an indefinite amount of recovery time, and the nominal entry state was chosen so that the landing ellipse fits within the UTTR and Woomera Test range boundaries. Therefore there is not a required timeline for the recovery procedures. Traditionally recovery occurs within 24 hours, and the experiment is returned for analysis within 72 hours.4[,7,6] Therefore this will be used as the baseline for the SPORE recovery procedures.

5 Conclusions

A Mission deigns architecture was constructed for the SPORE entry vehicle from capable of meeting the requirements set by multiple payloads, orbits, and vehicle sizes. Packaging models and mass budgets were created for the SPORE entry vehicles.3 DOF and 6 DOF Monte Carlo analyses verified that the selected architecture met all the requirements. A thermal soak-back analysis was used to generate a temperature profile for the payload. Results from the landing dispersion and thermal soak back analyses confirm Woomera, Australia as the current landing site and help establish recovery procedures.

In addition to progressing science, a primary goal of the SPORE team is to identify possible commercial payloads in order to increase accessibility to space. Ultimately SPORE provides a testbed to advance technologies and scientific knowledge required for future human and robotic explorations and the opportunity to increase commercialization in space.

References

1. D. A. Spencer and R. D. Braun, "Mars Pathfinder Atmospheric Entry: Trajectory Design and Dispersion Analysis", *Journal of Spacecraft & Rockets*, Vol. 33, No. 5, Sept-Oct. 1996, pp. 670-676.

2. D. A. Spencer, N. Bauer, J. Juneau, A. Willingham, A. Mandalia, M. Nehrenz, J. Kelly, and J. McClellan,"Small Probes for Orbital Return of experiments (SPORE) Final Report." 2012.

3. D. A. Spencer, N. Bauer, J. Juneau, A. Willingham, A.Mandalia, M. Nehrenz, J. Kelly, and J. McClellan, "SPORE Entry, Descent, and Landing." *50th AIAA Aerospace Sciences Meeting,* Nashville, 2012.

4. "European Users Guide to Low Gravity Platforms: Introduction to Foton Retrievable Capsules." *UIC-ESA-UM-0001* 2. Print.

5. G. L. Brauer et al., "Program To Optimize Simulated Trajectories (POST): Volume 1, Formulation Manual." Martin Marietta Corporation, 1990.

6. J. McGovern. "Stardust Returns Home." *Astronomy*. Astronomy News, 15 Jan. 2006. Web. 15 Mar. 2012. <http://www.astronomy.com/en/News-Observing/News/2006/01/Stardust%20returns%20home.aspx>.

7. JAXA HAYABUSA's Engine Turned Our Hopes into Reality." *JAXA*. Web. 15 Mar. 2012. <http://www.jaxa.jp/article/special/hayabusareturn/kuninaka01_e.html>.

8. M. Hinada, et. al., "Parachute System of MUSES-C Reentry Capsule," *CEAS/AIAA Aerodynamic Decelerator Systems Technology Conference, 15th,* Toulouse, France, 8-11 June 1999, Collection of Technical Papers (A99-30926 07-03).

9. R. A. Mitcheltree, C. M. Fremaux, and L. A. Yates, "Subsonic Static and Dynamic Aerodynamics of Blunt Entry Vehicles," AIAA 99-1020, *37th Aerospace Sciences Meeting and Exhibit*, Reno, NV, Jan. 1999.

10. R. A. Mitcheltree, S. Kellas, J. T. Dorsey, P. N. Desai and C. J. Martin, Jr., "A Passive Earth-Entry Capsule forMars Sample Return," 7th AIAA/ASME Joint Thermodynamics and Heat Transfer Conference, Albuquerque, NewMexico, AIAA 98-2851, June 15-18, 1998.

11. R. D. Braun, Mitcheltree, Robert A., and Cheatwood, F.M., "Mars Microprobe Entry Analysis," *NASA Langley Technical Report Server*, 1997.

12. R. R. Bate, D. D.Mueller, and J. E. White. Fundamentals of Astrodynamics. New York: Dover Publications, 1971. Print.

13. R.A. Mitcheltree, J. N. Moss, F.M.Cheatwood, F.A. Greene, and R. D. Braun, "Aerodynamics of the Mars Microprobe Entry Vehicles," AIAA Paper 97-3658, *Atmospheric Flight Mechanics Conference*, New Orleans, LA, August 11-13, 1997.

14. R.E.Otero and R.D Braun, "The Planetary Entry Systems Synthesis Tool: A Conceptual Design and Analysis Tool for EDL Systems*," IEEE Aerospace Conference Proceedings*, Paper No. 1331, Big Sky, MT, March 2010

15. S.A. Striepe et al., "Program To Optimize Simulated Trajectories (POST II): Volume 2, Utilization Manual." Martin Marietta Corporation, 2004.

16. T.W. Knacke, *Parachute Recovery Systems Design Manual*. 1st ed. Para Publications: Jan 1992.